

# **SEISMIC WAVE GENERATION AND PROPAGATION FROM COMPLEX 3D EXPLOSION SOURCES**

**Jeffry L. Stevens, et al.**

**Leidos  
10260 Campus Point Drive  
San Diego, CA 92121**

**28 April 2014**

**Final Report**

**APPROVED FOR PUBLIC RELEASE; DISTRIBUTION IS UNLIMITED.**



**AIR FORCE RESEARCH LABORATORY  
Space Vehicles Directorate  
3550 Aberdeen Ave SE  
AIR FORCE MATERIEL COMMAND  
KIRTLAND AIR FORCE BASE, NM 87117-5776**

## DTIC COPY

### NOTICE AND SIGNATURE PAGE

Using Government drawings, specifications, or other data included in this document for any purpose other than Government procurement does not in any way obligate the U.S. Government. The fact that the Government formulated or supplied the drawings, specifications, or other data does not license the holder or any other person or corporation; or convey any rights or permission to manufacture, use, or sell any patented invention that may relate to them.

This report was cleared for public release by the 377 ABW Public Affairs Office and is available to the general public, including foreign nationals. Copies may be obtained from the Defense Technical Information Center (DTIC) (<http://www.dtic.mil>).

AFRL-RV-PS-TR-2014-0084 HAS BEEN REVIEWED AND IS APPROVED FOR PUBLICATION IN ACCORDANCE WITH ASSIGNED DISTRIBUTION STATEMENT.

//SIGNED//

---

Robert Raistrick  
Project Manager, AFRL/RVBYE

//SIGNED//

---

Glenn M. Vaughan, Colonel, USAF  
Chief, Battlespace Environment Division

This report is published in the interest of scientific and technical information exchange, and its publication does not constitute the Government's approval or disapproval of its ideas or findings.

REPORT DOCUMENTATION PAGE				Form Approved OMB No. 0704-0188	
Public reporting burden for this collection of information is estimated to average 1 hour per response, including the time for reviewing instructions, searching existing data sources, gathering and maintaining the data needed, and completing and reviewing this collection of information. Send comments regarding this burden estimate or any other aspect of this collection of information, including suggestions for reducing this burden to Department of Defense, Washington Headquarters Services, Directorate for Information Operations and Reports (0704-0188), 1215 Jefferson Davis Highway, Suite 1204, Arlington, VA 22202-4302. Respondents should be aware that notwithstanding any other provision of law, no person shall be subject to any penalty for failing to comply with a collection of information if it does not display a currently valid OMB control number. <b>PLEASE DO NOT RETURN YOUR FORM TO THE ABOVE ADDRESS.</b>					
1. REPORT DATE (DD-MM-YYYY) 28-04-2014		2. REPORT TYPE Final Report		3. DATES COVERED (From - To) 29 March 2011 to 28 March 2014	
4. TITLE AND SUBTITLE Seismic Wave Generation and Propagation from Complex 3D Explosion Sources				5a. CONTRACT NUMBER FA9453-11-C-0232	
				5b. GRANT NUMBER	
				5c. PROGRAM ELEMENT NUMBER 62601F	
6. AUTHOR(S) Jeffrey L. Stevens, Thomas W. Thompson, and Michael O'Brien				5d. PROJECT NUMBER 1010	
				5e. TASK NUMBER PPM00009359	
				5f. WORK UNIT NUMBER EF004045	
7. PERFORMING ORGANIZATION NAME(S) AND ADDRESS(ES) Leidos 10260 Campus Point Drive San Diego, CA 92121				8. PERFORMING ORGANIZATION REPORT NUMBER	
9. SPONSORING / MONITORING AGENCY NAME(S) AND ADDRESS(ES) Air Force Research Laboratory Space Vehicles Directorate 3550 Aberdeen Avenue SE Kirtland AFB, NM 87117-5776				10. SPONSOR/MONITOR'S ACRONYM(S) AFRL/RVBYE	
				11. SPONSOR/MONITOR'S REPORT NUMBER(S) AFRL-RV-PS-TR-2014-0084	
12. DISTRIBUTION / AVAILABILITY STATEMENT  Approved for public release; distribution is unlimited. (377ABW-2014-0339 dtd 15 May 2014)					
13. SUPPLEMENTARY NOTES					
14. ABSTRACT  We are investigating generation of complex seismic waves by explosions in media with realistic 3D heterogeneity, including topography and tectonic strain release. We have developed a 3D nonlinear finite element code CRAM3D designed for calculation of explosions in 3D heterogeneous media with well-tested material models and including gravity; and implemented interface codes using the representation theorem that propagate the numerical solution from the source region to regional and teleseismic distances. We simulated the nonproliferation experiment (NPE) including the effects of surface topography. We added the capability to calculate explosions with tectonic strain release. We specifically model the nuclear explosion Shoal. Shoal is in an area with northwest extension, which amplifies motion in that direction. Waveforms from the 3D calculation of Shoal are consistent with observed near field waveforms and surface wave radiation patterns. We also calculate far-field body waves and find that tectonic release has very little effect on far-field P-wave amplitudes, although it does generate SH waves not present in the calculation without tectonic release. This implies that while tectonic release may significantly affect Ms, the effect on mb will be small.					
15. SUBJECT TERMS nonlinear finite element calculations, nuclear explosion monitoring, Tectonic Strain Release, Nonproliferation Experiment, Shoal					
16. SECURITY CLASSIFICATION OF:			17. LIMITATION OF ABSTRACT	18. NUMBER OF PAGES	19a. NAME OF RESPONSIBLE PERSON
a. REPORT Unclassified	b. ABSTRACT Unclassified	c. THIS PAGE Unclassified			Robert Raistrick
			Unlimited	58	19b. TELEPHONE NUMBER (include area code)

This page is intentionally left blank.

## Table of Contents

1. SUMMARY .....	1
2. INTRODUCTION .....	1
3. TECHNICAL APPROACH.....	2
3.1 The CRAM3D Code .....	2
3.2 Propagation with the Elastodynamic Representation Theorem .....	3
3.3 Incorporation of Tectonic Prestress .....	3
3.4 Incorporation of Topography .....	4
4. RESULTS AND DISCUSSION .....	5
4.1 Calculation of the NPE .....	5
4.2 Calculation of Shoal.....	14
4.2.1 Shoal: Near Field Waveforms.....	15
4.2.2 Shoal: Regional Waveforms and Surface Waves .....	17
4.2.3 Shoal: Long Period Surface Waves .....	19
4.2.4 Shoal: Far Field Body Waves .....	22
4.2.5 Shoal: Hypothetical Compressive Prestress.....	27
4.3 3D Earth Heterogeneity .....	30
4.3.1 Heterogeneous Source Region: Far Field Body Waves.....	33
4.3.2 Heterogeneous Source Region: Broadband Waveforms and Surface Waves..	36
4.3.3 Heterogeneous Source Region: Nonlinear Deformation .....	39
5. CONCLUSIONS.....	42
REFERENCES .....	43
LIST OF SYMBOLS, ABBREVIATIONS, AND ACRONYMS .....	45

## List of Figures

Figure 1. The CRAM 3D finite element outer grid (left) is rectangular. The inner grid (center) is shaped to match the shape of the explosion shock wave. CRAM2D uses a similar axisymmetric spider grid (right) in the region around the explosion. ....	2
Figure 2. Stress regimes vary by region. Horizontal stresses may be substantially larger or smaller than the vertical stress. ....	4
Figure 3. From left to right, vertical, eastward and northward displacements caused by topography along a slice 204 meters from the NPE shot point.....	5
Figure 4. Topography around the area of the NPE calculation (top left) and the topography on the CRAM grid surface (top right). Lower figure shows a Google Earth image with a line due north from directly above the explosion to the edge of the grid. ....	6
Figure 5. Left: Pressure field along a vertical slice 120 meters from the origin at 6 times: 0.05, 0.1, 0.2, 0.3, 0.5 and 1.0 seconds. Note the strong interactions between the shock wave and both the free surface topographic features and material layer boundaries. Right: final nonlinear deformation along a cross section through the source showing regions of yielding and tensile cracking. ....	7
Figure 6. Comparison of calculated and observed waveforms from the NPE on the surface at three locations: ground zero, immediately above the explosion, and at distances of 264 and 670 meters. Note the distinct spall phase that decreases in duration with distance in both the data and the calculation. ....	7
Figure 7. Shot level calculated and observed waveforms at a distance of 500 meters. Observed tangential motion is most likely off-axis radial and/or vertical motion. Blue line: NPE data, Green line: calculated velocity without topography, Red line: calculated velocity with topography. ....	8
Figure 8. Full topography (top) and tapered topography (bottom) together with calculated Tangential/Radial amplitude ratio. Tangential component data is generated particularly at topographic gradients.....	10
Figure 9. Tangential/Radial amplitude ratio calculated with topography (top) and data (bottom) using the early part of the waveform. Agreement is fairly good within the region where topography is explicitly modeled indicating that the early time tangential component data on the surface most likely is caused by topography.....	11
Figure 10. Full near-field surface waveforms and locations within the grid. The large SH at the bottom two stations that is not matched by the calculation resembles an inverted P-wave and is most likely a P-wave that has reflected from the surface and then from the dipping intermediate layer back to the surface. ....	12
Figure 11. Calculated and observed waveforms from the NPE at station ELK at a distance of 400 km. Top: Observed; Middle: calculated with topography; Bottom: calculated with flat topography. ....	13
Figure 12. Location of the Shoal explosion and the three near-field shot level recording stations and the direction of the local stress state. The extensional stress $Sh_{min}$ is the west-northwest direction, which is the direction from the origin to PM-3. The second principal stress is harder to determine and in the calculation we model it as slightly compressive.....	14
Figure 13. Vertical and horizontal stresses used in the calculation shown vs. depth. Dashed lines indicate the critical stress limited by balance against friction.....	14

Figure 14. Source function for material properties used in the Shoal calculation calculated using a 1D spherically symmetric code and using a shot level free-field waveform from Cram3D. Left: spectral amplitude; Right: RVP time series. ....	15
Figure 15. Observed near field (shot level) velocity (left) and displacement (right) at the three Shoal stations. ....	16
Figure 16. Left: observed displacement waveforms at the three shot-level Shoal recording stations. Right: calculations with prestress in the directions of maximum ( $Az=0$ ) and minimum ( $Az=90$ ) horizontal stress. Both data and calculations show enhanced late time displacements in the direction of minimum principal stress.....	17
Figure 17. CRAM3D calculation of Shoal without prestress propagated to 250 km using the representation theorem. These are broadband full waveform seismograms calculated using wavenumber integration. Seismic waveforms are independent of observation direction. ....	18
Figure 18. CRAM3D calculation of Shoal with tectonic prestress propagated to 250 km using the representation theorem. Now there is a love wave and variability in the Rayleigh wave with azimuth. Zero degrees is the direction of extension. ....	18
Figure 19. CRAM3D calculation of Shoal with prestress propagated to 250 km using fundamental mode Rayleigh and Love wave Green's functions low pass filtered at 0.1 Hz. Rayleigh waves vary in amplitude with angle and a Love wave is generated. ....	19
Figure 20. From Lambert, Flynn and Archambeau (1972). The Rayleigh and Love wave radiation pattern observed from the Shoal explosion is consistent with the calculation. ....	20
Figure 21. Left: Fundamental mode Rayleigh and Love wave spectra from the Shoal calculation with prestress at 250 km. Right: Calculation without prestress plus point moment tensor solution as discussed in the text. ....	20
Figure 22. Comparison of 1D and 3D surface wave spectra. All are fundamental mode spectra at a distance of 250 km. The black dashed line labeled "3D" is the spectrum from the 3D calculation <i>without</i> tectonic release. The black dotted line is from a 1D calculation convolved with the spherically symmetric source function multiplied by 1.4. The three colored curves are 1D point source calculations constrained to have the same long period limit as the 3D calculation, but with different values of $M_{zz}$ vs. $M_{xx}$ and $M_{yy}$ as discussed in the text. ....	21
Figure 23. P waves from Shoal calculation with tectonic release (black) and without (red). There are very small differences in the waveforms. Units are velocity normalized to $4 \times 10^{-4}$ m/s. TOA is takeoff angle from the vertical. N, NE and E indicate the direction to the receiver as discussed in the text. ....	22
Figure 24. SV waves from Shoal calculation with tectonic release (black) and without (red). There are very small differences in the waveforms. Units are velocity normalized to $4 \times 10^{-4}$ m/s.....	23
Figure 25. SH waves from Shoal calculation with tectonic release (black) and without (red). In the NE direction, a substantial SH wave is generated in the calculation with tectonic release that is not present in the calculation without tectonic release. Again, units are velocity normalized to $4 \times 10^{-4}$ m/s, but note that the limits are different from the previous figures. The SH wave in the NE direction is about 10% the size of the SV waves. SH is zero in the north and east directions.....	23

Figure 26. Top row: Far field P waves in the X and Y directions – X (North) is the direction of extension. Bottom row: Velocity differences subtracting the waveform without prestress from the waveform with prestress. Both are for a 30 degree takeoff angle. Units are velocity normalized to $4 \times 10^4$ m/s. ....	24
Figure 27. Top row: Far field SV waves in the X and Y directions – X (North) is the direction of extension. Bottom row: Velocity differences subtracting the waveform without prestress from the waveform with prestress. Both are for a 30 degree takeoff angle. Units are velocity normalized to $4 \times 10^4$ m/s. ....	25
Figure 28. Far field SH-waves calculated at 10 (left), 20 (middle) and 30 (right) degree take-off angles from Shoal calculations with and without prestress; 45 degrees from the direction of extension. ....	25
Figure 29. Far field P-waves calculated for a spherically symmetric explosion source (red) compared with far field P-waves from the Shoal calculation without tectonic release (black). Both calculations used the same material properties and earth structure. From left to right, take-off angles of 10, 20 and 30 degrees. ....	26
Figure 30. Far field SV-waves calculated for a spherically symmetric explosion source (red) compared with far field SV-waves from the Shoal calculation without tectonic release (black). Both calculations used the same material properties and earth structure. From left to right, take-off angles of 10, 20 and 30 degrees. ....	26
Figure 31. Stress state for calculation of Shoal with compressive prestress. The dashed line is the critical SHmax stress limited by friction. ....	27
Figure 32. Broadband waveforms from the Shoal calculation with compressive prestress. .	28
Figure 33. Fundamental mode waveforms at 250 km from the calculation with compressive prestress low pass filtered at 0.1 Hz. The bottom row shows the waveforms from the Shoal calculation described in the previous section degrees for comparison. Surface wave amplitude for the compressive case in the direction of compressive prestress is reduced. ....	28
Figure 34. Top row: Far field P waves in the X and Y directions – X (North) is the direction of extension. Bottom row: Velocity differences subtracting the waveform without prestress from the waveforms with the Shoal prestress and hypothetical compressive prestress. Both are for a 30 degree takeoff angle. Units are velocity normalized to $4 \times 10^4$ m/s. ....	29
Figure 35. Top row: Far field SV waves in the X and Y directions – X (North) is the direction of extension. Bottom row: Velocity differences subtracting the waveforms without prestress from the waveforms with the Shoal prestress and hypothetical compressive prestress. Both are for a 30 degree takeoff angle. Units are velocity normalized to $4 \times 10^4$ m/s. ....	29
Figure 36. Far field SH-waves calculated at 10 (left), 20 (middle) and 30 (right) degree take-off angles from Shoal calculations without prestress and the waveforms with the Shoal prestress and hypothetical compressive prestress; 45 degrees from the direction of extension. ....	30
Figure 37. Taken from Shiomi et al. 1997: Well logs showing P- and S-wave velocities and mass density versus depth for well YT2 in Kyushu, Japan for depths of 600 m to 1710 m. ....	31
Figure 38. <i>Top panels</i> : Examples of the randomly generated material property distributions for one set of the “lithosphere” calculations for a 2 km × 2 km horizontal	



slice at 100 m depth. The resolution (cell size) of the material property distribution is 20 m. The statistical properties of these distributions are identical to those in well YT2.	
<i>Bottom panels.</i> Same as the top panels, but for the “modified lithosphere” calculations.....	31
Figure 39. The distributions of the properties derived from the YT2 well log data. ....	32
Figure 40. <i>Left panel:</i> Autocorrelation function of P wave velocity, S wave velocity, and density of the data from well YT2. The numerals are the mean-squared fractional fluctuation for each property. <i>Middle panel:</i> Ensemble average of the autocorrelation functions of bulk modulus, shear modulus, and density used in the “lithosphere” calculations. <i>Right panel:</i> Same as the middle panel, but for the “modified lithosphere” calculation. ....	32
Figure 41. <i>Top:</i> Body waves for a 10 degree take-off angle, low-pass filtered at 20 Hz, for 4 directions for each of the 3 “lithosphere” calculations. The amplitudes of the waveforms are scaled by $1e-4$ and are for 1000 km range. Time is on the $x$ -axis; a negative offset of 0.333 s has been applied to the shear waves to align the start of the motion. <i>Middle:</i> Same as the top panel, but for the 3 “weakened lithosphere” calculations. <i>Bottom:</i> Same as the top panels, but with the “uniform” media calculation subtracted from the waveforms. ....	34
Figure 42. Normalized power spectral density of the body waves for the 4 types of scenarios under investigation. Distinct wave types (take-off angles) are shown in each row (column).....	36
Figure 43. Surface wave displacements in 4 directions at 250 km range for the “lithosphere 1” calculation. The waveforms are low-pass filtered at 2 Hz. The $y$ -axis is measured in units of $1e-6$ m for horizontal displacements and $1e-7$ m for vertical displacements.....	37
Figure 44. Same as Figure 43, but for the “lithosphere 1 (weakened)” calculation. ....	37
Figure 45. Normalized power spectral density of the surface waves for displacements in the horizontal, vertical, and radial planes (top to bottom). The right panel shows the power spectra after smoothing in frequency, created by averaging the power in adjacent frequency bins to more clearly show the spectral differences between the waveforms. ....	38
Figure 46. Difference in normalized spectral power for the surface waves with and without enhanced material weakening.....	39
Figure 47. Vertical plane through the shot point showing nonlinear damage in the source region comprised of uniform material properties. Cells that have yielded are shown in blue, and cells that have cracked are shown in red. ....	40
Figure 48. <i>Top and middle panels:</i> Vertical plane through the shot point showing nonlinear deformation in the source region for the “lithosphere 1” and “lithosphere 1 (weakened)” calculations, respectively. <i>Bottom panel:</i> Vertical plane through the shot point showing the shear modulus.....	40
Figure 49. Same as Figure 48, but for the “modified lithosphere 1” calculations. ....	41
Figure 50. Regions of enhanced weakening (smoothed with a Gaussian kernel of 20 m half-width) for the “lithosphere 1” calculation (left) and the “modified lithosphere 1” calculation (right) in the $x$ - $y$ plane at shot depth. Overlaid on top of the images are contours enclosing the regions of nonlinear deformation. Each image is 600 m on a side. Colors span 0.35 to 0.65, indicating the fractional strength of the material relative to the non-weakened calculations. ....	42

## List of Tables

Table 1. NPE region earth model.....	13
Table 2. Elastic properties used in the Shoal calculation.....	15
Table 3. Nine 3D finite element calculations were performed to investigate 3D Heterogeneity. ....	31
Table 4. RMS amplitudes of body waves for the nine CRAM3D calculations.....	35
Table 5. Azimuthal variation (percent) of body waves in the presence of heterogeneity (1 $\sigma$ ) .....	35
Table 6. Surface waves with uniform and heterogeneous material properties in the source region. ....	37

## **Acknowledgment**

We thank Steve Myers of Lawrence Livermore National Laboratories for providing the 3D earth model and topography for the NPE site.

This page is intentionally left blank.

## 1. SUMMARY

We are investigating generation of complex seismic waves by explosions in media with realistic 3D heterogeneity, including topography and tectonic strain release. We have developed a 3D nonlinear finite element code designed for calculation of explosions in 3D heterogeneous media with well-tested material models and including gravity; and implemented interface codes using the representation theorem that propagate the numerical solution from the source region to regional and teleseismic distances.

We have run calculations of the NPE with and without topography, and extended the calculation to 400 km using the representation theorem. The calculation shows that the effect of topography can be modeled and produces effects consistent with the data. Near field tangential motion is caused primarily by topographic gradients. The effect of near-source topography on subsurface ground motion is primarily due to off-axis propagation. The effects of near-source topography on far-field seismic radiation are small.

We perform calculations of the nuclear test SHOAL with and without tectonic strain release. The calculation shows that tectonic strain release consistent with the local stress state can generate near field and regional signals, including long period surface waves, similar to those observed. We find that tectonic release causes small changes to the far-field P-wave waveform, but has very little effect on far-field P-wave amplitudes. It does generate SH waves not present in the calculation without tectonic release. This implies that while tectonic release may significantly affect  $M_s$ , the effect on  $m_b$  will be small. We also find that nonlinear deformation caused by free surface interaction increases the  $M_{zz}$  component of the source, adding a CLVD component. However, the free surface interaction also increases the  $M_{xx}$  and  $M_{yy}$  components and the net effect on surface wave amplitudes is small.

We use available information on structural heterogeneity to develop 3D models that have the statistical characteristics of the upper few kilometers of the earth's crust. We modified the Shoal earth model to have these statistical characteristics. We ran a series of calculations first varying the elastic properties of the structure, but keeping strength the same, and second modifying the strength to vary as a function of shear modulus. The extra degree of freedom provided in three dimensions makes generation of shear waves easier than with the restriction to axisymmetric geometry. All of calculations with the heterogeneous structure generated shear waves not present in the initial plane-layered structure, however the effect is much stronger with strength variation.

## 2. INTRODUCTION

This project follows a previous project on 3D numerical modeling and wave propagation. In that project, we did the following:

1. Developed a 3D nonlinear finite element code designed for calculation of explosions in 3D heterogeneous media with well-tested material models and including gravity;
2. Implemented interface codes using the representation theorem that propagate the numerical solution from the source region to regional and teleseismic distances;
3. Used the code to evaluate the effect of near source heterogeneity including non-linear material property variations, elastic variability and topography.

The reason that 3D calculations are important for understanding shear wave generation is that symmetry constraints imposed by 1D and 2D calculations act to suppress shear waves. Imposition of 2D axisymmetry requires that the motion generated by the explosion be identical in all horizontal directions through propagation of the shock wave, nonlinear deformation of the surrounding material, and rebound to a final state. Since the motion is never identical in all directions, shear waves will always be generated, and in fact shear waves are observed from all underground explosions. In this project we are attempting to develop realistic representative models for 3D near-source heterogeneity, followed by 3D explosion calculations in these models. We have performed calculations for two specific events: the Non-Proliferation Experiment (NPE) and the Shoal underground nuclear test. For the NPE, we included the topography above and near the explosion. For Shoal, we included tectonic prestress corresponding to the stress state for that location in Nevada.

### 3. TECHNICAL APPROACH

#### 3.1 The CRAM3D Code

CRAM 3D is an explicit three-dimensional Lagrangian finite element code designed to run on multiple processors (Stevens and Xu, 2010; Stevens et al, 2011; Stevens et al, 2014). For an explosion simulation, the cavity is placed near the center of the grid and is enclosed by a spider grid which facilitates applying the pressure boundary condition and rezoning elements (Figure 1). The well-tested nonlinear material models from CRAM 2D have been implemented in CRAM 3D. The code includes gravity and so includes the important effects that result from variation of overburden pressure with depth. Gravitational equilibrium is established by running an initial calculation with no source, followed by a second calculation including the explosion source. We have also implemented the capability to include tectonic prestress in the calculations.

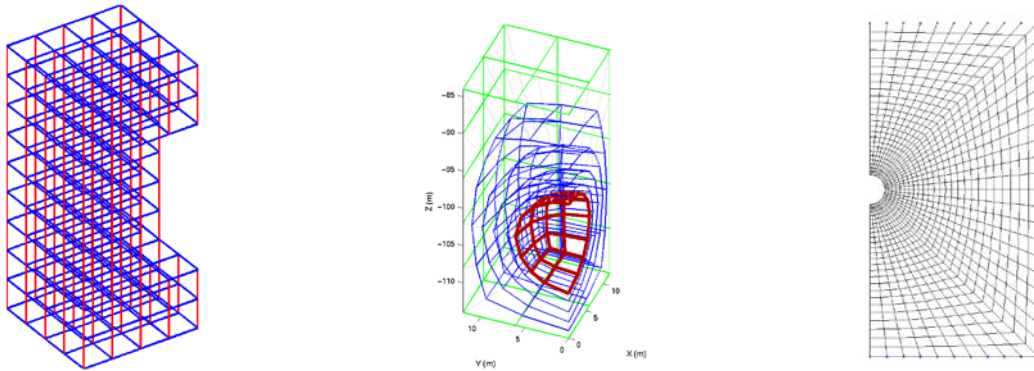


Figure 1. The CRAM 3D finite element outer grid (left) is rectangular. The inner grid (center) is shaped to match the shape of the explosion shock wave. CRAM2D uses a similar axisymmetric spider grid (right) in the region around the explosion.

### 3.2 Propagation with the Elastodynamic Representation Theorem

The representation theorem allows us to perform arbitrarily complex nonlinear calculations in the source region, and then propagate them with an appropriate Green's function. The representation theorem is exact. That is, no matter how complex the 3D motion is on the source region boundary, it will be correctly propagated by the representation theorem. The only exception is that it will not calculate the interaction of backscattered waves reflected from outside the source region with complexities of the source region.

In the three-dimensional numerical finite difference calculations, we save displacements and stresses (or velocities and stress rates) due to the seismic source on a monitoring surface on the boundary of a rectangle (5 planar surfaces, excluding the upper surface), and calculate Green's functions from each point on the monitoring surface to the receiver and so the synthetic seismogram at the receiver point  $X$  outside of the monitoring surface is obtained by integrating over the monitoring surface  $S_M$

$$u_i(X) = \int_{S_M} \left\{ G_j^i(\xi; X) * T_j^M(\xi) - u_j^M(\xi) * S_{jk}^i(\xi; X) n_k \right\} dA \quad (1)$$

in the frequency domain, where  $G_j^i(\xi; X)$  and  $S_{jk}^i(\xi; X)$  are the Green's function and the stress tensor on the monitoring surface due to a unit impulsive force at  $X$  in direction  $i$ ,  $T_j^M$  is the traction on the monitoring surface due to the seismic source,  $u$  is the displacement on the monitoring surface, and  $n$  is the normal to the monitoring surface. The operator  $*$  denotes convolution and the summation convention is assumed.

We use a plane-layered Green's function outside the source region. The Green's functions for the complete seismograms are derived from an algorithm based on the work of Luco and Apsel (1983) and Apsel and Luco (1983). The technique used for surface waves is similar to the method of Bache et al. (1982). The Green's functions for body waves are generated by a procedure similar to that described by Bache and Harkrider (1976) using a saddle point approximation to calculate a far-field plane wave for a given takeoff angle from a source in a plane-layered medium. Although the full waveform Green's functions generate the complete waveform, the other Green's functions provide additional insight into the source and waveform generation.

### 3.3 Incorporation of Tectonic Prestress

The effect of tectonic prestress on explosion-generated surface waves has been discussed in many prior studies (e.g., Archambeau, 1972; Rygg, 1979; Toksoz and Kehler, 1972). In most of these studies tectonic release was modeled as superposition of a tectonic source described by a double couple, multipole or moment tensor source, plus a point explosion source. The size of the tectonic source was determined by comparison with the observed Love waves and Rayleigh wave radiation pattern. Day et al. (1987) first attempted to perform numerical modeling of tectonic release through an axisymmetric calculation of the explosion Piledriver. Murphy et al. (2011, 2013) performed similar calculations for the North Korean explosions. To the best of our knowledge no one has previously performed numerical calculations for a three-dimensional stress field.

The first step in performing a calculation of tectonic release is to determine the stress state of the earth. While the stress state varies between regions, considerable work has also been done on this subject (e.g., Zoback, 2010). In general the vertical stress is equal to the overburden weight of the material above at any given point. The horizontal stresses may be larger or smaller than this value up to the point where failure due to frictional sliding or rock fracturing relieves the stress. In most of the earth's crust tectonic stresses are applied continuously, and so the prestress is in general close to equilibrium with frictional sliding. The ratio of maximum to the minimum principal stress, both reduced by pore pressure, is given by

$$\frac{S_{\max} - P_p}{S_{\min} - P_p} = \left[ \mu + (\mu^2 + 1)^{\frac{1}{2}} \right]^2 \quad (2)$$

where  $\mu$  is the coefficient of friction,  $P_p$  is the pore pressure,  $S_{\max}$  is the maximum of the vertical stress  $S_v$  and the maximum horizontal stress  $SH_{\max}$  and  $S_{\min}$  is the minimum of  $S_v$  and the minimum horizontal stress  $Sh_{\min}$ . For a typical coefficient of friction of 0.6, this ratio is 3.1, so the difference between principal stresses can be substantial and the effect on seismic waves potentially large. In our calculations, we calculate the overburden weight to determine the vertical stress, and then modify the horizontal stresses to some fraction of the frictional limit. This is the initial stable state of the calculation prior to introduction of the explosion. Note that although the vertical stress is still equivalent to the overburden weight, the pressure is not, and it may be either increased or reduced by the tectonic stresses. Since material strength increases with pressure, this also can substantially affect the seismic source. In general, normal faulting regimes will amplify seismic signals, while reverse faulting regimes will decrease seismic signals; strike-slip regimes could do either (Figure 2).

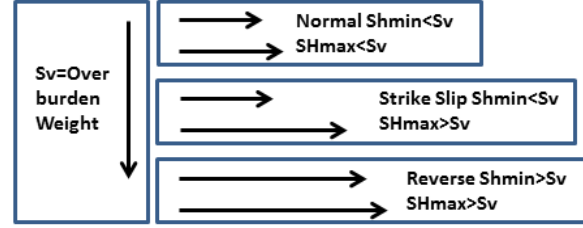


Figure 2. Stress regimes vary by region. Horizontal stresses may be substantially larger or smaller than the vertical stress.

### 3.4 Incorporation of Topography

CRAM3D incorporates topography by gradually distributing offsets of the grid from top to bottom so that change in cell dimensions is gradual rather than abrupt at the surface. The main difficulty in implementing topography is establishing gravitational equilibrium. The variation in overburden pressure with depth is very important in nonlinear calculations because strength is pressure dependent and so material becomes much weaker at shallow depths. Because of this we need to bring the grid into gravitational equilibrium before running an explosion calculation. As mentioned above, this is done by starting with an approximate solution for overburden pressure in the grid and then running an initial calculation without the explosion. While this can be accomplished relatively easily for a plane-layered structure, bringing the grid to gravitational equilibrium in a structure with significant topography has proven to be difficult. While the calculation will eventually come to equilibrium, adding topography is the equivalent of dropping a mountain onto the free surface, and so it takes quite a long time to come to equilibrium. We have experimented with several approximate solutions (e.g., Liu and Zoback, 1992), but have not



as yet found a solution that allows the equilibrium run to be completed without taking considerable time. The calculated displacements caused by topography close to the NPE calculation are shown in Figure 3.

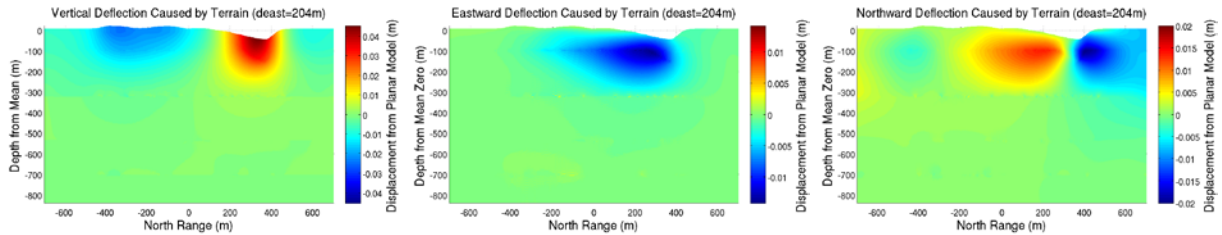


Figure 3. From left to right, vertical, eastward and northward displacements caused by topography along a slice 204 meters from the NPE shot point.

## 4. RESULTS AND DISCUSSION

### 4.1 Calculation of the NPE

As our first calculation of a historical event with 3D heterogeneity, we model the Non-Proliferation Experiment (NPE), including the surface topography. The NPE was a chemical explosion with yield equivalent to one kiloton of TNT. The explosive is 1.315 kilotons of a 50/50 ANFO/emulsion mix in a cylindrical cavity centered at 389 m depth, 7.7 m in radius (horizontally) and 5.2m in height (vertically). We previously modeled this event in a two-dimensional axisymmetric calculation (Stevens et al, 2004), and initially used the same material properties, which were derived from Rimer et al (1994) for the 3D calculation. The material geology at the NPE site is based on that of the nearby Misty Echo event and consists of four layers. Layers 1 and 4 are non-porous, and layers 2 and 3 have porosities of 3% and 0.5% respectively. Comparison of the initial calculations with recordings from this event showed that calculated arrival times were early relative to the data, so porous moduli in the material were reduced so that P-velocities were more consistent with the observed arrival times, similar to material velocities used by Kamm and Bos (1995).

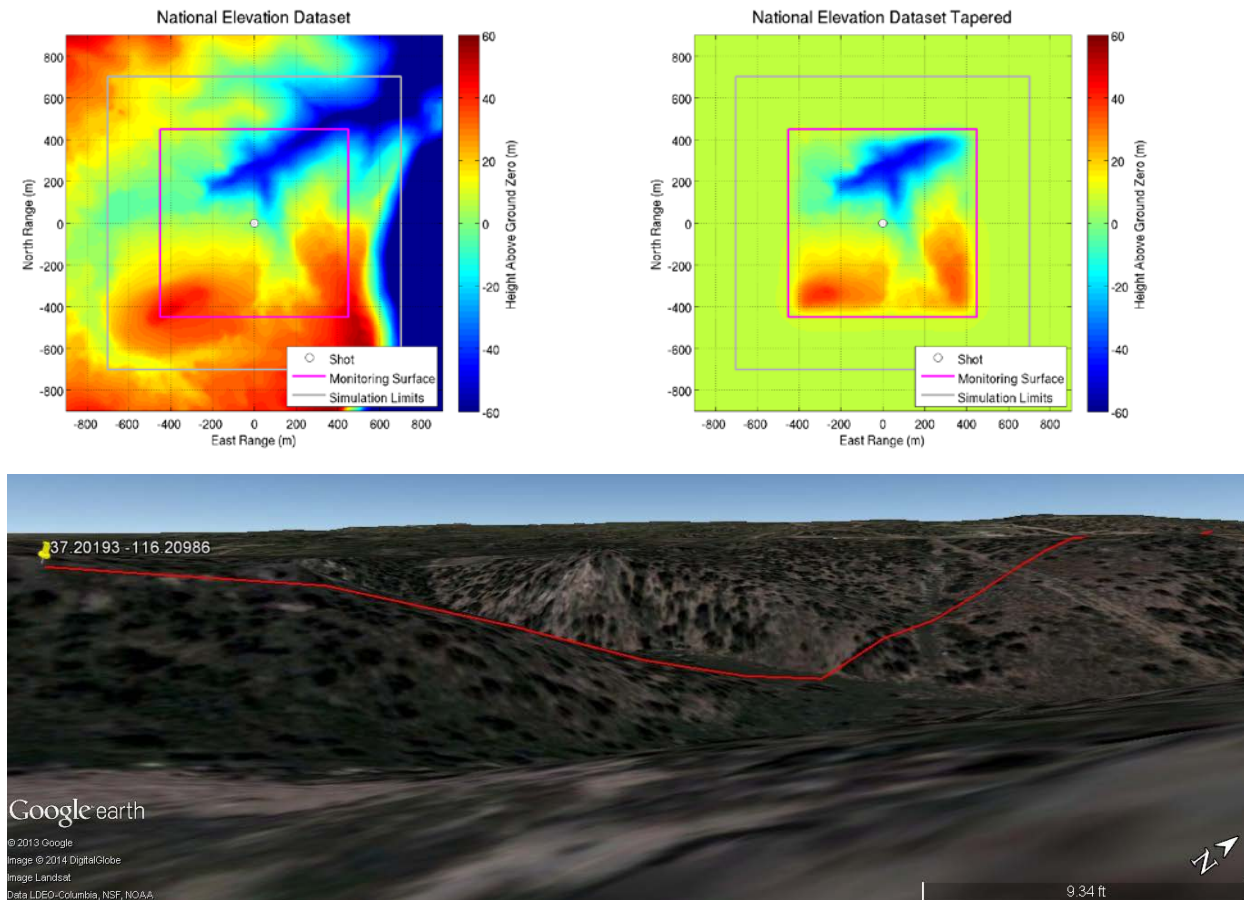


Figure 4. Topography around the area of the NPE calculation (top left) and the topography on the CRAM grid surface (top right). Lower figure shows a Google Earth image with a line due north from directly above the explosion to the edge of the grid.

Figure 4 shows the actual topography near the NPE (National Elevation Dataset 1/3 Arc-Second <http://seamless.usgs.gov/ned13.php>). For this calculation, we modeled the area within 650 meters of the explosion. Even that relatively small area has substantial topography, with elevation differences of up to 140 meters. The strongest topographic changes are along a canyon to the north and a ridge to the south. The calculation area is tapered at the edges to bring it to a constant elevation at and outside the monitoring surface that is used to propagate the calculation as described above.

Figure 5 (left) shows the pressure field output from the calculation with topography at several times. The upgoing shock wave interacts with the surface in a complicated way causing distortion of the reflected waves. Figure 5 (right) shows the region of nonlinear deformation and tensile cracking. Nonlinear deformation near the explosion is approximately spherical, but elongated and slightly offset vertically. The region of cracking is confined to near the free surface. This explosion is deeply overburied, so there is less asymmetry than in a normally buried explosion.

Figure 6 shows the calculated and observed velocity waveforms at three points on the free surface. Spall is indicated by a linear trending velocity with a slope of  $g$ , and is readily apparent

in the ground zero waveform and also visible in the more distant surface stations. The match between calculated and observed waveforms is quite good.

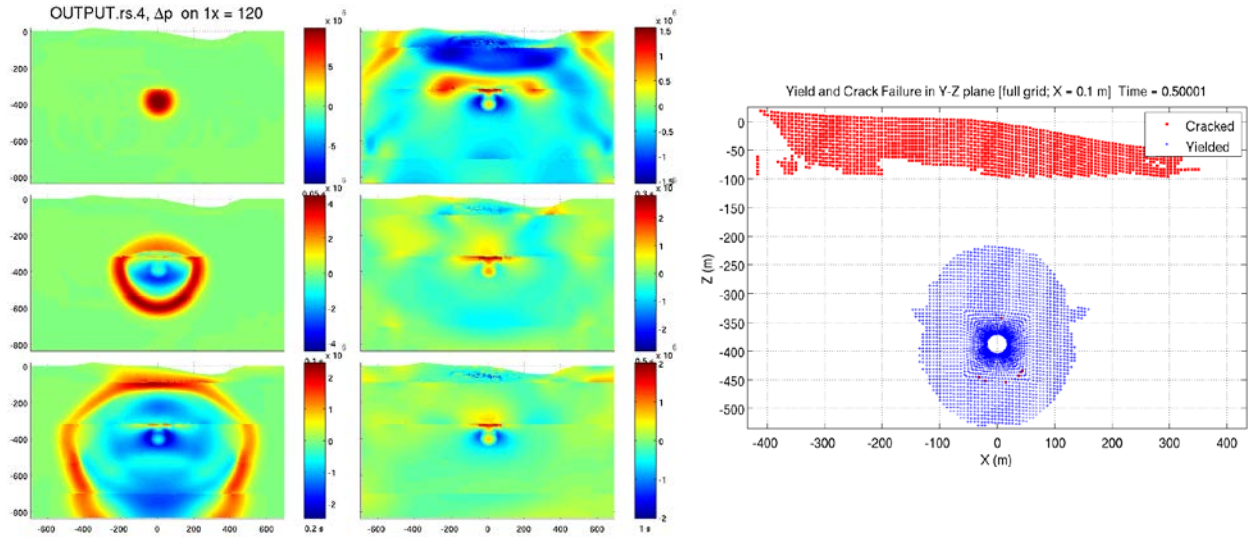


Figure 5. Left: Pressure field along a vertical slice 120 meters from the origin at 6 times: 0.05, 0.1, 0.2, 0.3, 0.5 and 1.0 seconds. Note the strong interactions between the shock wave and both the free surface topographic features and material layer boundaries. Right: final nonlinear deformation along a cross section through the source showing regions of yielding and tensile cracking.

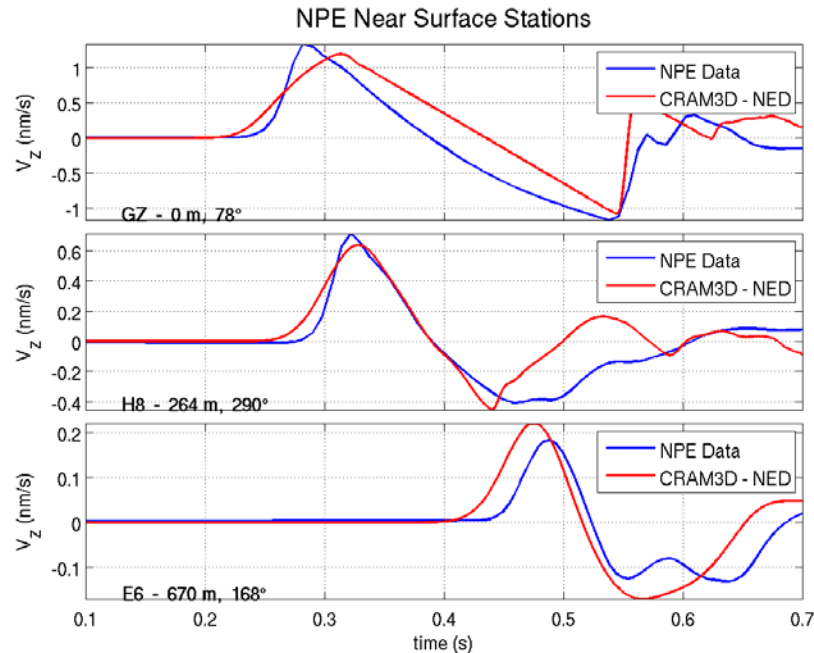


Figure 6. Comparison of calculated and observed waveforms from the NPE on the surface at three locations: ground zero, immediately above the explosion, and at distances of 264 and 670 meters. Note the distinct spall phase that decreases in duration with distance in both the data and the calculation.

In order to assess the effect of topography distinct from other mechanisms that might affect waveforms, we also ran a calculation with flat topography. In general the results are not very different. With topography there is some tangential motion not present in the flat calculation and small differences in waveforms, but the differences are not significant except on the surface near topographic gradients. Figure 7 shows a comparison of near field observed and calculated waveforms at shot depth. In a uniform medium only the radial component would be nonzero. However, the free surface interaction causes a large arrival on the vertical component at about 0.7 seconds. Neither the flat nor topographic calculation predicts significant tangential motion at this location. Although there is motion on the tangential component, the clear P arrival and strong resemblance to the vertical component suggests that the motion is mostly off-axis vertical or radial motion rather than true tangential motion.

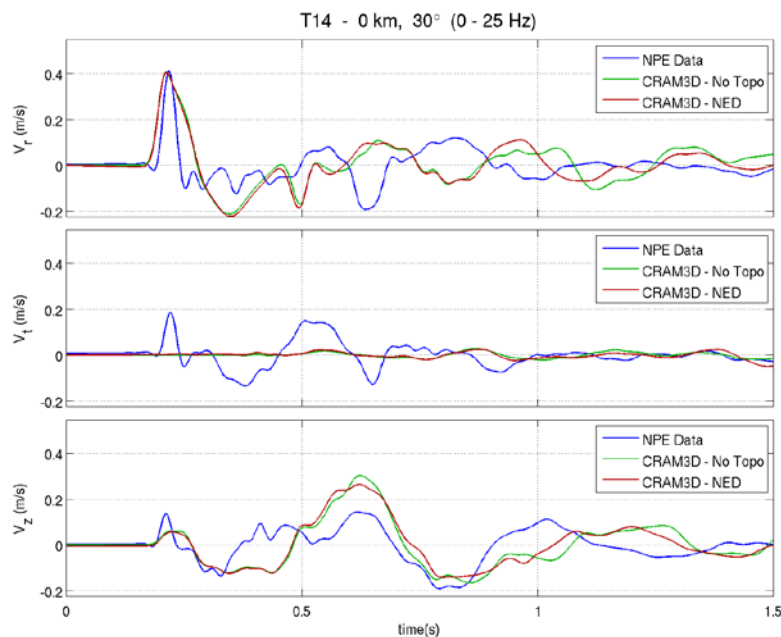


Figure 7. Shot level calculated and observed waveforms at a distance of 500 meters. Observed tangential motion is most likely off-axis radial and/or vertical motion. Blue line: NPE data, Green line: calculated velocity without topography, Red line: calculated velocity with topography.

The strongest effect of topography is on surface stations, and so we compared our results with the observed ground motion at those locations. Figure 8 shows the calculated tangential/radial component amplitude ratio on the surface above the explosion at the locations where stations were placed during the event. Note that the tangential component amplitudes correlate with topographic gradients. That is, locations where the surface elevation changes rapidly generates tangential motion. Figure 9 shows a comparison of the observed and calculated tangential/radial motion using the first part of the observed waveforms at each station. The agreement is quite good, confirming that surface topography is likely responsible for the tangential motion observed. Figure 10 shows a more detailed comparison of the calculated and observed data over a longer time period. The agreement is reasonably good. Spall, for example, is modeled quite well. The main difference is in the large SH observed at later times at some of the stations

(bottom three stations in the seismogram plot). Note the strong resemblance of the phase to an inverted direct P-wave. There is also a large velocity contrast in the earth model just above the source, and there is some slope to these earth layers that we are not modeling in our calculations. Our conclusion from this is that the large anomalous “SH” motion is actually P-wave that has reflected off the surface, then back up off the reflecting, dipping layers so that it is no longer vertically polarized and appears on the tangential component.

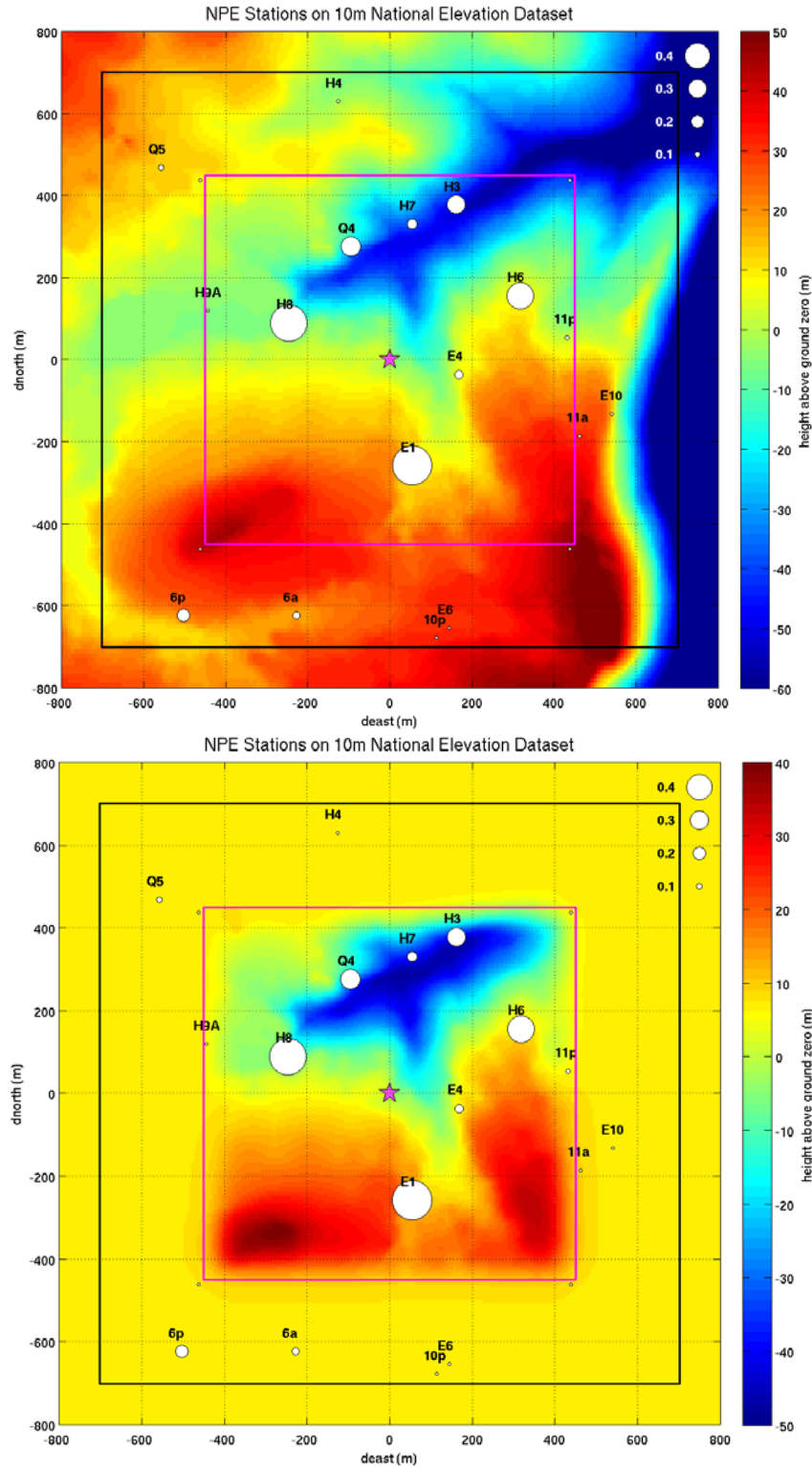


Figure 8. Full topography (top) and tapered topography (bottom) together with calculated Tangential/Radial amplitude ratio. Tangential component data is generated particularly at topographic gradients.



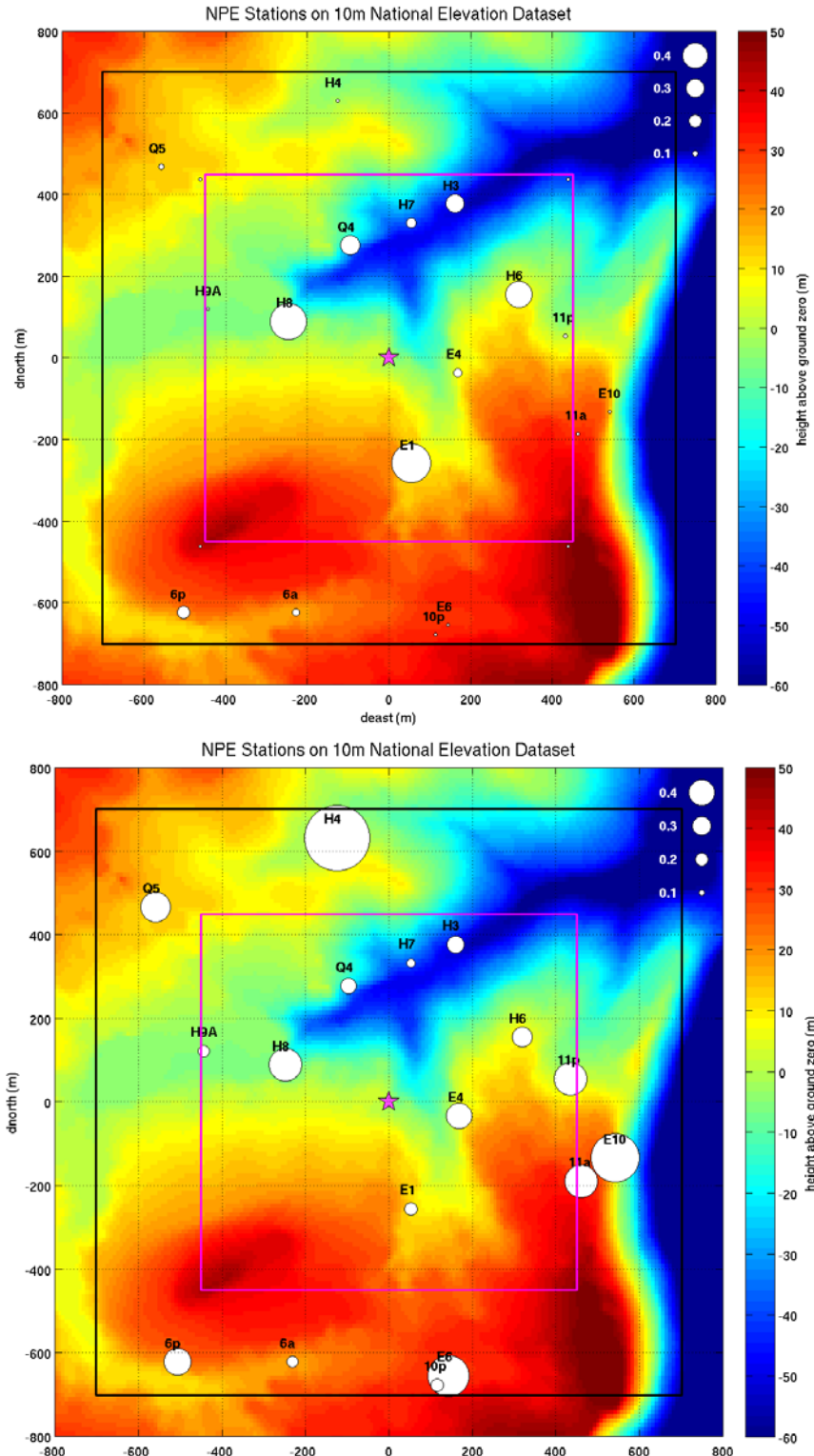


Figure 9. Tangential/Radial amplitude ratio calculated with topography (top) and data (bottom) using the early part of the waveform. Agreement is fairly good within the region where topography is explicitly modeled indicating that the early time tangential component data on the surface most likely is caused by topography.

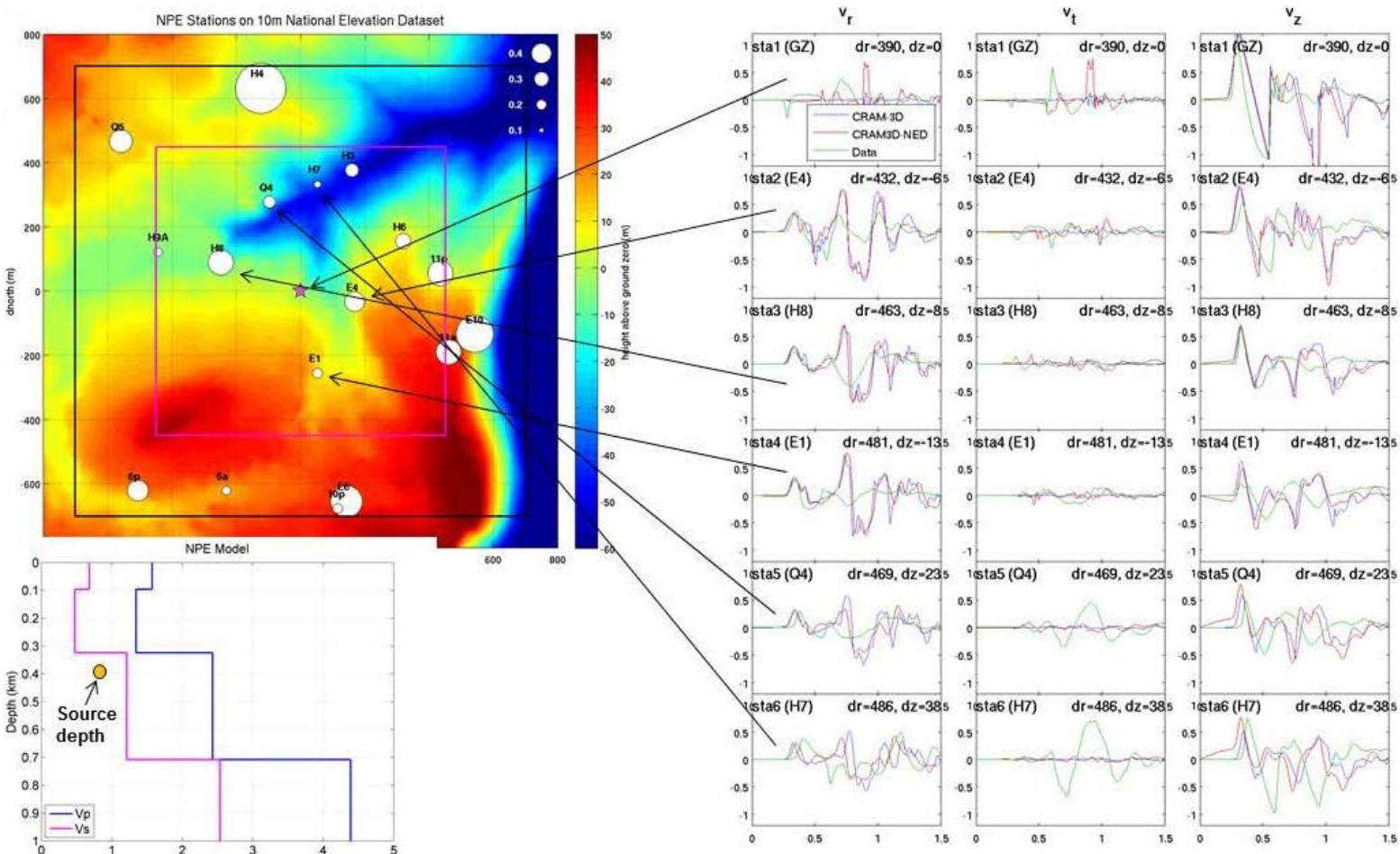


Figure 10. Full near-field surface waveforms and locations within the grid. The large SH at the bottom two stations that is not matched by the calculation resembles an inverted P-wave and is most likely a P-wave that has reflected from the surface and then from the dipping intermediate layer back to the surface.



We used the representation theorem to calculate waveforms for comparison with observations at a number of locations. We used an earth model derived by merging the local NPE model of Rimer et al (1994), and the regional 3D model of Myers et al (2007) (Table 1). The Q structure used in the calculation is based on Swanger's Law,  $Q=\beta/10$  where  $\beta$  is shear velocity. The calculated and observed waveforms at ELK are shown in Figure 11. The waveforms are generally similar, and the relative P and S amplitudes are quite good. Arrival times are earlier in the observations than the calculation, indicating that the structure used is somewhat slower than the actual earth structure between the NPE and ELK. Near field topography does not have a noticeable effect on the waveforms at this distance.

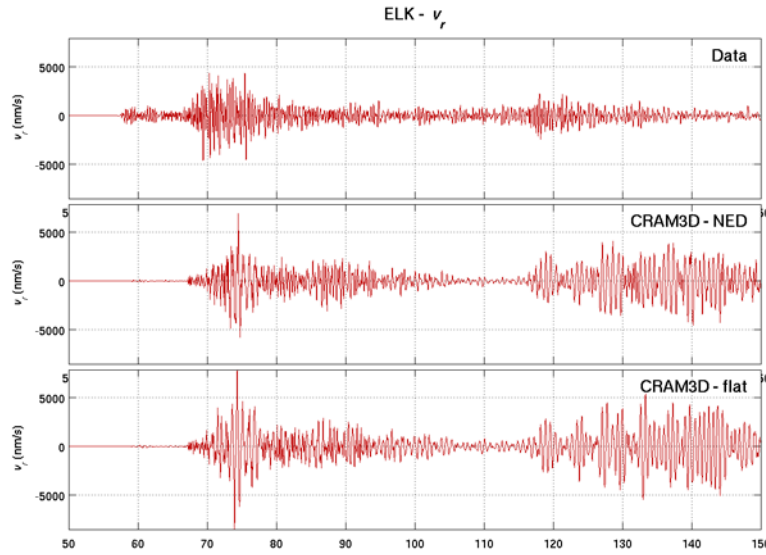


Figure 11. Calculated and observed waveforms from the NPE at station ELK at a distance of 400 km. Top: Observed; Middle: calculated with topography; Bottom: calculated with flat topography.

Table 1. NPE region earth model

Depth (km)	Thickness (km)	Vp (km/sec)	Vs (km/sec)	Density (gm/cc)	Q
0.102	0.102	3.586	1.809	2.200	180
0.328	0.226	1.824	1.000	1.663	100
0.704	0.376	2.701	1.357	1.900	140
3.600	2.896	3.210	1.900	1.680	190
3.660	0.060	4.500	2.600	2.300	260
8.100	4.440	5.930	3.500	2.430	350
12.240	4.140	5.950	3.510	2.453	351
14.280	2.040	5.970	3.520	2.458	352
17.280	3.000	6.000	3.540	2.467	354
20.280	3.000	6.070	3.580	2.487	358
23.280	3.000	6.200	3.660	2.523	366
26.220	2.940	6.310	3.720	2.554	372
29.220	3.000	6.360	3.750	2.568	375
34.740	5.520	6.410	3.780	2.582	378
37.260	2.520	7.900	4.400	3.001	440

## 4.2 Calculation of Shoal

Shoal was a 12.5 kiloton nuclear explosion detonated near Fallon, Nevada at 367 m depth (Weart, 1965). There were three near-field shot level recording stations located in three directions each at about 590 meters from the shot (Figure 12). The minimum principal stress  $Sh_{min}$  in this part of Nevada is in extension. It is unclear from regional tectonics whether the maximum horizontal stress  $SH_{max}$  is less than or greater than the vertical stress  $S_v$ . For the purpose of this calculation, we made  $SH_{max}$  20% larger than  $S_v$ , and made  $Sh_{min}$  95% of the critical stress corresponding to frictional sliding with a coefficient of friction of 0.6. The stress state in the upper kilometer is shown in Figure 13.

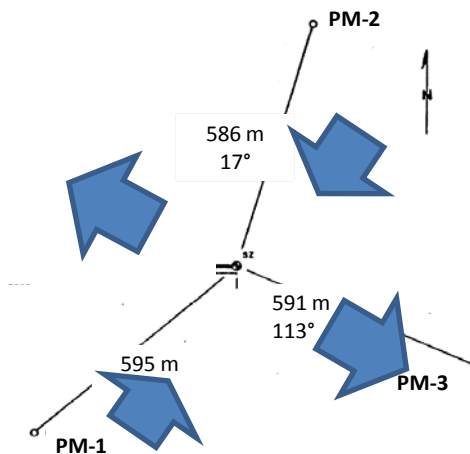


Figure 12. Location of the Shoal explosion and the three near-field shot level recording stations and the direction of the local stress state. The extensional stress  $Sh_{min}$  is the west-northwest direction, which is the direction from the origin to PM-3. The second principal stress is harder to determine and in the calculation we model it as slightly compressive.

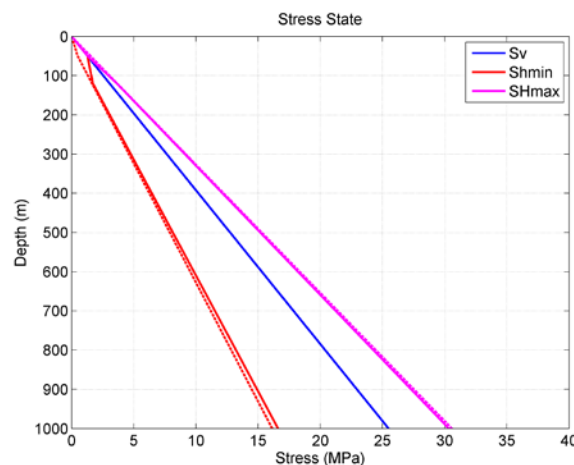


Figure 13. Vertical and horizontal stresses used in the calculation shown vs. depth. Dashed lines indicate the critical stress limited by balance against friction.

Elastic material properties used in the calculation were derived from Beers (1964) and are listed in Table 2. The same material was used throughout the grid, assuming negligible porosity and uniform strength. Initial strength corresponded to fractured granite, and strength reduction was modeled using a shear strain based shock damage model derived for Piledriver granite (Stevens et al, 2003). The grid used in the calculation was 2 km x 2 km by 0.8 km deep with 10 meter spacing. The initial cavity was 4.32 meters in radius and the inner grid spacing started at 0.5 meters, gradually increasing to the exterior grid spacing.

Table 2. Elastic properties used in the Shoal calculation

Density	2600 kg/m <sup>3</sup>
P-velocity	5175 m/s
S-velocity	3026 m/s

Figure 14 shows time domain RVP and source spectra calculated in two ways, first with a 1D spherically symmetric code and second with CRAM3D derived from the first second of a radial waveform at shot level. The results are similar, but the 3D code breaks the perfect symmetry of the spherically symmetric calculation, causing reduced rebound and extending motion over a longer time period. This causes a less peaked spectrum and higher static level.

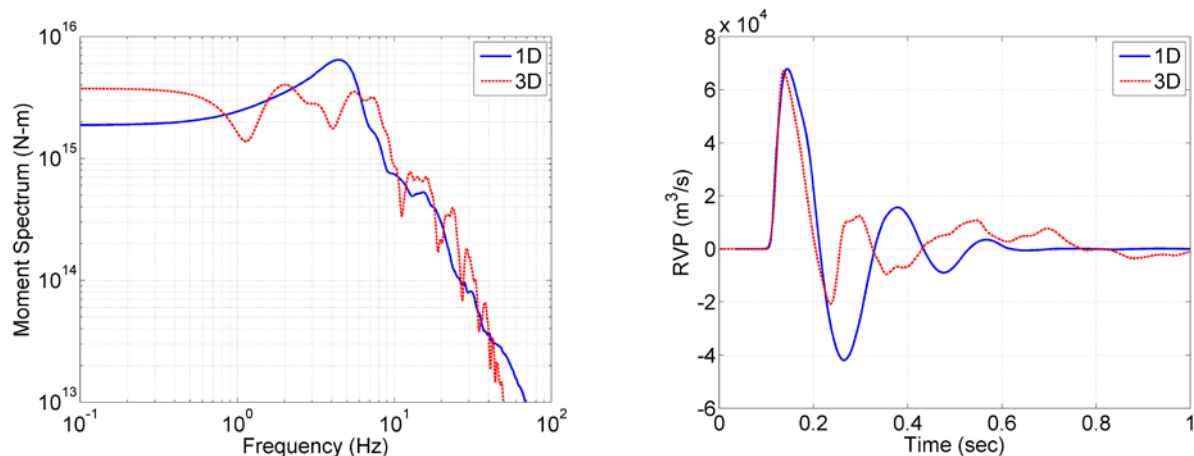


Figure 14. Source function for material properties used in the Shoal calculation calculated using a 1D spherically symmetric code and using a shot level free-field waveform from Cram3D. Left: spectral amplitude; Right: RVP time series.

#### 4.2.1 Shoal: Near Field Waveforms

Figure 15 shows the observed shot level radial ground motion at the three stations described above and shown in Figure 12. The motion is very different at the three stations. In particular station PM-3 had a large positive final displacement, while at the other two stations the final displacement was small, and in fact slightly negative at PM-1.

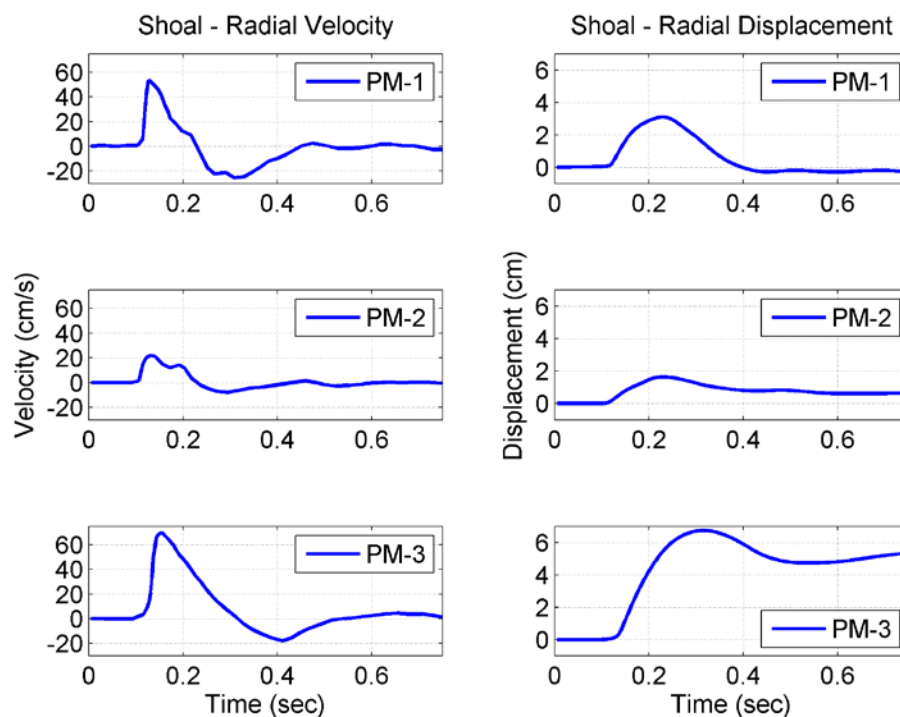


Figure 15. Observed near field (shot level) velocity (left) and displacement (right) at the three Shoal stations.

Figure 16 shows the displacement waveforms observed at the three stations compared with calculated waveforms at the same depth in the directions of minimum and maximum horizontal stress. As noted above, one of the surprising aspects of the data from this event is the strong directionality of the shot-level seismic waveforms, in particular the fact that the final displacements were so different at the three stations. We see a similar effect in our calculations. The late time displacement is amplified in the direction of minimum principal stress compared to the other directions (smaller than the observations, but otherwise very consistent). PM-3, the station with the largest displacement, is in the direction of the regional tectonic minimum principal stress, so prestress is very likely a strong contributor to the differences in the observed displacements.

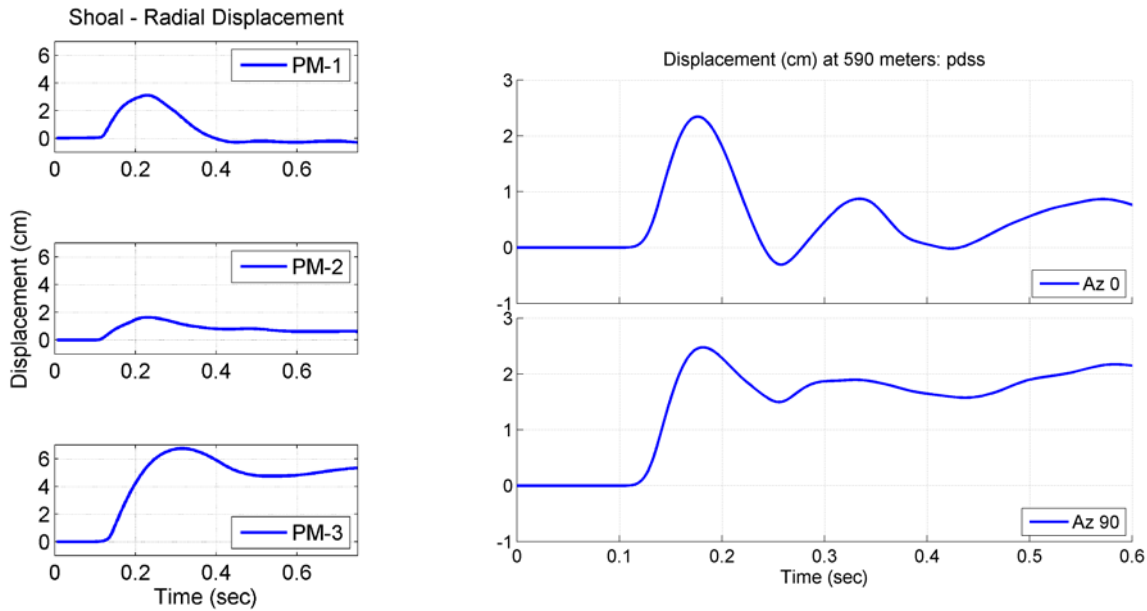


Figure 16. Left: observed displacement waveforms at the three shot-level Shoal recording stations. Right: calculations with prestress in the directions of maximum ( $Az=0$ ) and minimum ( $Az=90$ ) horizontal stress. Both data and calculations show enhanced late time displacements in the direction of minimum principal stress.

#### 4.2.2 Shoal: Regional Waveforms and Surface Waves

We calculated regional waveforms using full waveform Green's functions at 250 km distance from two calculations, the first with no tectonic stress and the second with tectonic stress as described above. In the calculation without tectonic release, the seismic radiation is isotropic and there is no motion on the tangential component (Figure 17). However, with tectonic release a strong Love wave is generated and the Rayleigh waves have a radiation pattern, with amplitudes increased in the direction of extensional stress and decreased in the direction of (smaller) compressive stress (Figure 18). Note that although tectonic release causes variability in the Rayleigh waves and tangential motion not present at all without it, the regional body waves are not significantly altered by tectonic release.

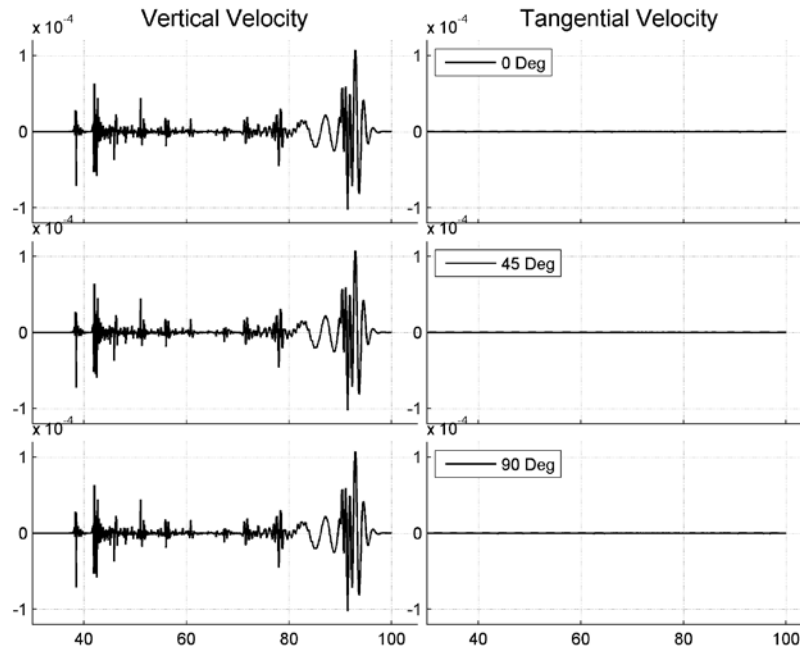


Figure 17. CRAM3D calculation of Shoal without prestress propagated to 250 km using the representation theorem. These are broadband full waveform seismograms calculated using wavenumber integration. Seismic waveforms are independent of observation direction.

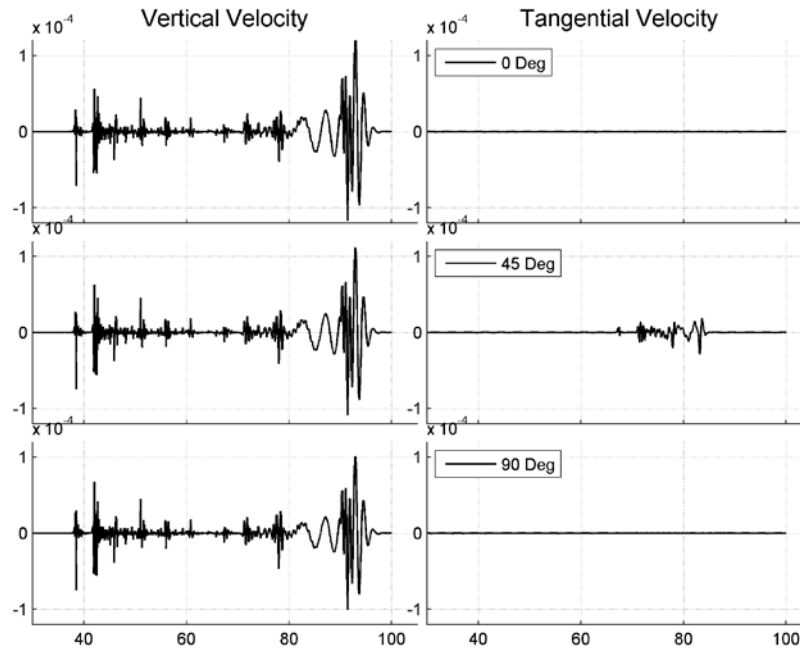


Figure 18. CRAM3D calculation of Shoal with tectonic prestress propagated to 250 km using the representation theorem. Now there is a love wave and variability in the Rayleigh wave with azimuth. Zero degrees is the direction of extension.

### 4.2.3 Shoal: Long Period Surface Waves

To see the long period behavior more clearly, we generated seismograms using the representation theorem with fundamental mode surface wave Green's functions. A problem occurs when trying to apply the representation theorem to long period surface waves. The Green's function for a vertical force becomes large at long periods, so any small vertical motion left in the grid is amplified and dominates the signal. In fact, this term must vanish in the long period limit. To resolve this problem we extend the time series by 0.1 seconds and adjust the stresses on the side and bottom so that the total force and impulse on the monitoring surface is zero at the end of the calculation. This problem was described for axisymmetric problems and a similar technique applied by Bache et al. (1982).

Fundamental mode surface waves calculated at 250 km and low pass filtered at 0.1 Hz are shown in Figure 19. The Rayleigh wave is increased in amplitude by about 60% in the direction of extension compared to the direction of (mild) compression. A Love wave is generated with maximum amplitude about half of the Rayleigh wave amplitude. We compared the Rayleigh and Love waves with observations of surface waves by Lambert, Flynn and Archambeau (1972) and found that the calculations are consistent with the observed radiation pattern (Figure 20). Although the observed effect appears to be larger than the calculated effect, the radiation pattern clearly shows amplification in the direction of extension and a Love wave radiation pattern consistent with the Rayleigh wave radiation pattern.

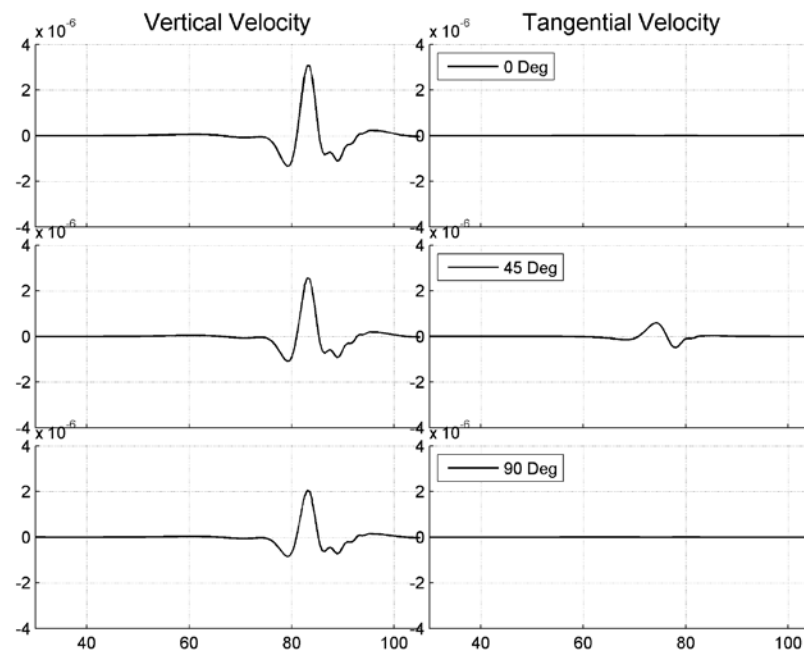


Figure 19. CRAM3D calculation of Shoal with prestress propagated to 250 km using fundamental mode Rayleigh and Love wave Green's functions low pass filtered at 0.1 Hz. Rayleigh waves vary in amplitude with angle and a Love wave is generated.

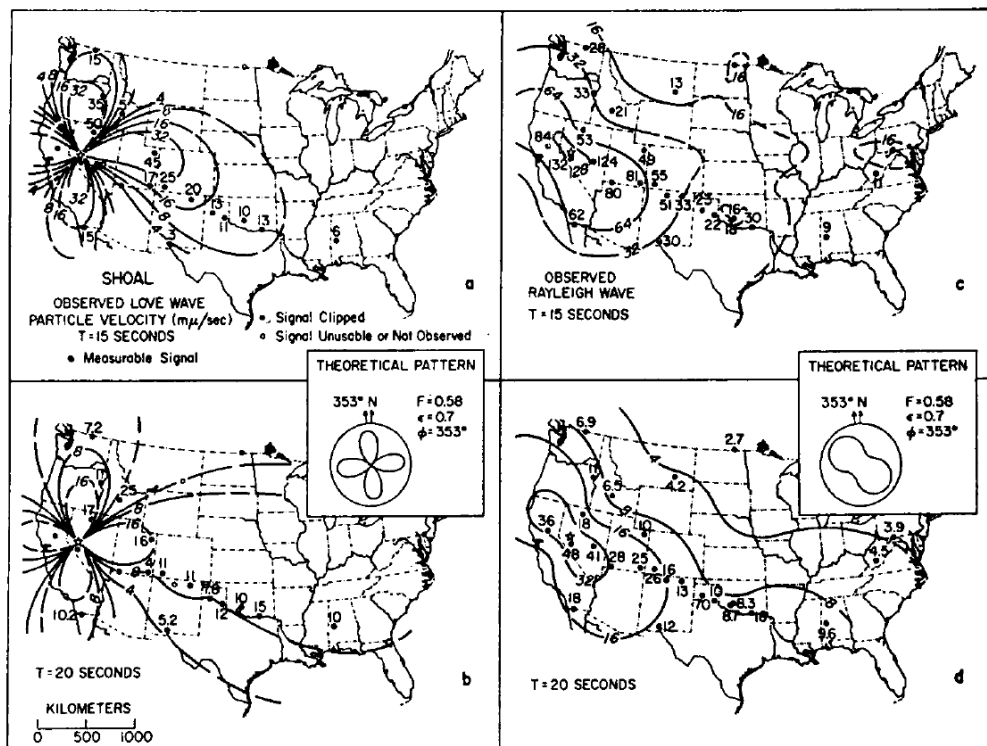


Figure 20. From Lambert, Flynn and Archambeau (1972). The Rayleigh and Love wave radiation pattern observed from the Shoal explosion is consistent with the calculation.

We can estimate the size of the calculated tectonic source by comparing the surface waves for the calculations with and without prestress. We find that a moment tensor with  $M_{xx}=7.5 \times 10^{14}$  and  $M_{yy}=-2.5 \times 10^{14}$  added to the calculation without prestress matches the Love wave and the Rayleigh wave variation for the calculation with prestress very well (Figure 21). The isotropic moment for the 1D calculation in the same material (Figure 14) had a moment of  $1.9 \times 10^{15}$ , so the perturbation in the horizontal components is about half of the isotropic moment.

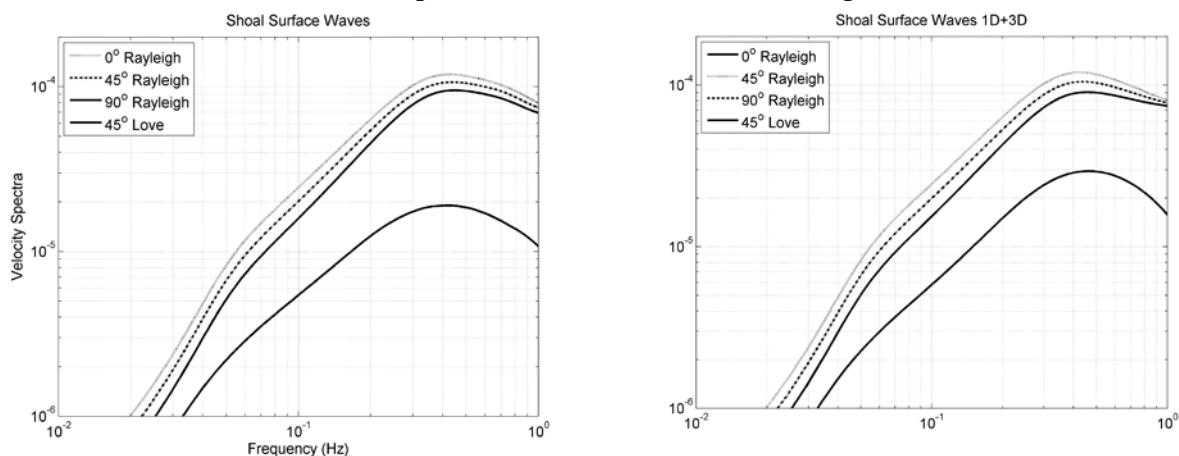


Figure 21. Left: Fundamental mode Rayleigh and Love wave spectra from the Shoal calculation with prestress at 250 km. Right: Calculation without prestress plus point moment tensor solution as discussed in the text.



We can take this analysis a bit further and determine the effect of the free surface on the vertical and horizontal moment tensor components. Figure 22 shows a comparison of surface wave spectra from the 3D calculation compared with spectra from several 1D calculations. The isotropic moment of the 3D source is well defined by the long period limit of the surface wave spectrum and is equal to  $2.6 \times 10^{15}$  N-m. As discussed earlier, there is more overshoot in the 1D than the 3D source which reduces the low frequency level (Figure 14), so we multiply the spectrum from the point explosion source convolved with the 1D source function by 1.4 to make the long period levels the same. At frequencies below 0.1 Hz, all of the spectra are indistinguishable and consistent with an isotropic point source solution. At higher frequencies ( $\sim 0.4$  Hz) there is a divergence of the spectra for two reasons: in the 1D case it is because of the spectral shape caused by rebound; in the 3D case it is because of the free surface interaction. The spectra can be matched by increasing the  $M_{zz}$  component and also increasing the  $M_{xx}$  and  $M_{yy}$  components by a lesser amount. The red curve in the figure, which fits the full spectral shape quite well, has  $M_{zz}$  increased by a factor of 2.5 over the apparent isotropic moment, while  $M_{xx}$  and  $M_{yy}$  are increased by a factor of 1.5, so the final moment tensor is  $M_{zz}=6.4 \times 10^{15}$ ,  $M_{xx}=M_{yy}=3.8 \times 10^{15}$ . The isotropic moment increases to  $4.67 \times 10^{15}$  and there is a CLVD component caused by the difference between the horizontal and vertical stresses. This is similar to the “damage” mechanism that has been discussed by Patton and Taylor (2011). Note, however, that although the CLVD caused by the free surface interaction reduces the surface wave amplitude, the isotropic moment is also increased and so the net effect on the surface wave amplitude is small. The surface wave generated by the 1D source is actually smaller by a factor of 1.4 than the 3D solution as discussed above, but a direct comparison is not possible because the overshoot in the 1D case causes the surface wave amplitude to be lower, and that effect is reduced in the 3D case.

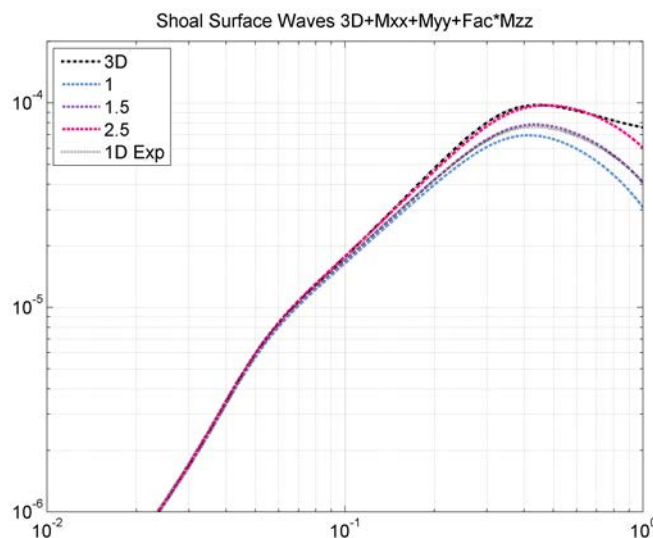


Figure 22. Comparison of 1D and 3D surface wave spectra. All are fundamental mode spectra at a distance of 250 km. The black dashed line labeled “3D” is the spectrum from the 3D calculation *without* tectonic release. The black dotted line is from a 1D calculation convolved with the spherically symmetric source function multiplied by 1.4. The three colored curves are 1D point source calculations constrained to have the same long period limit as the 3D calculation, but with different values of  $M_{zz}$  vs.  $M_{xx}$  and  $M_{yy}$  as discussed in the text.

#### 4.2.4 Shoal: Far Field Body Waves

We calculated far-field body waves from the Shoal calculations with and without tectonic release to examine the effect on body wave signatures and generation of S waves. The results show only small differences in the P and SV waves (SV waves are primarily generated by P to S conversion at the free surface), however tectonic release generates a far-field SH wave that is absent in the case without tectonic release. Figure 23, Figure 24 and Figure 25 show P, SV and SH waves calculated in the North, Northeast and East directions, where North is the direction of extension in the calculation. All waveforms were calculated at a distance of 1000 km in a granite half space and were filtered with a causal low pass filter at 5 Hz. All waveforms are downgoing waves as if they were measured 1000 km below the source in a perfect granite medium undisturbed by reflections (other than above the source) or mantle complexity, so these waveforms provide a very clear image of the seismic source.

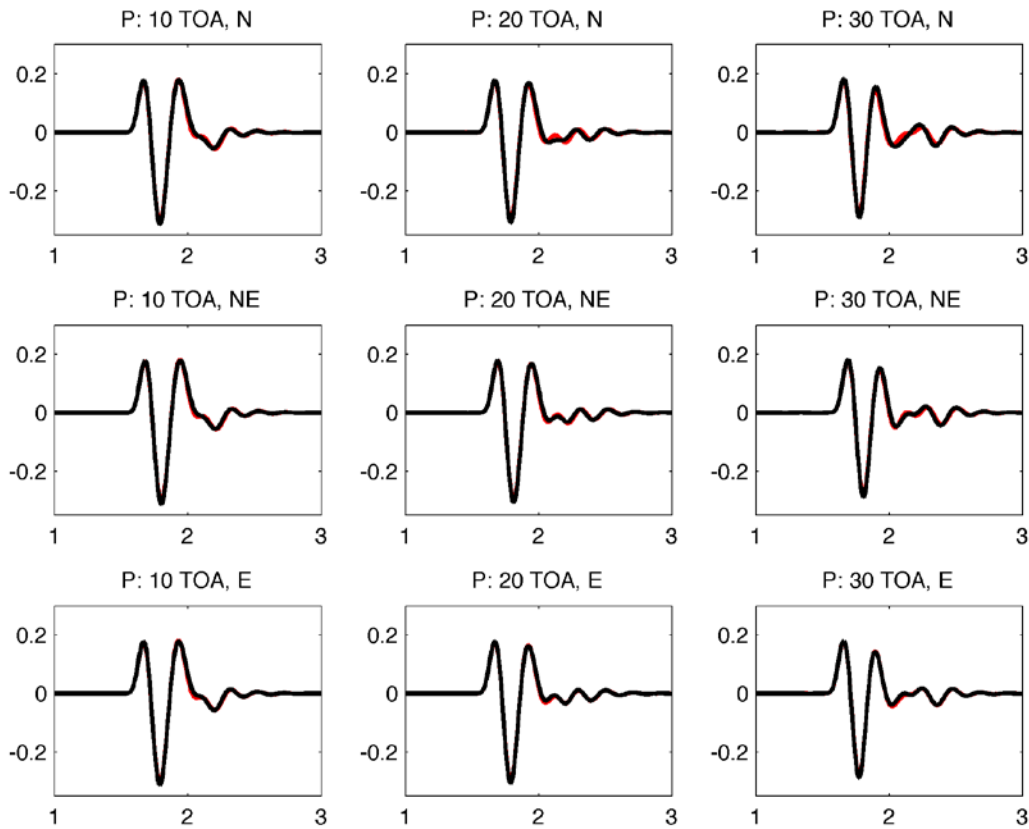


Figure 23. P waves from Shoal calculation with tectonic release (black) and without (red). There are very small differences in the waveforms. Units are velocity normalized to  $4 \times 10^{-4}$  m/s. TOA is takeoff angle from the vertical. N, NE and E indicate the direction to the receiver as discussed in the text.

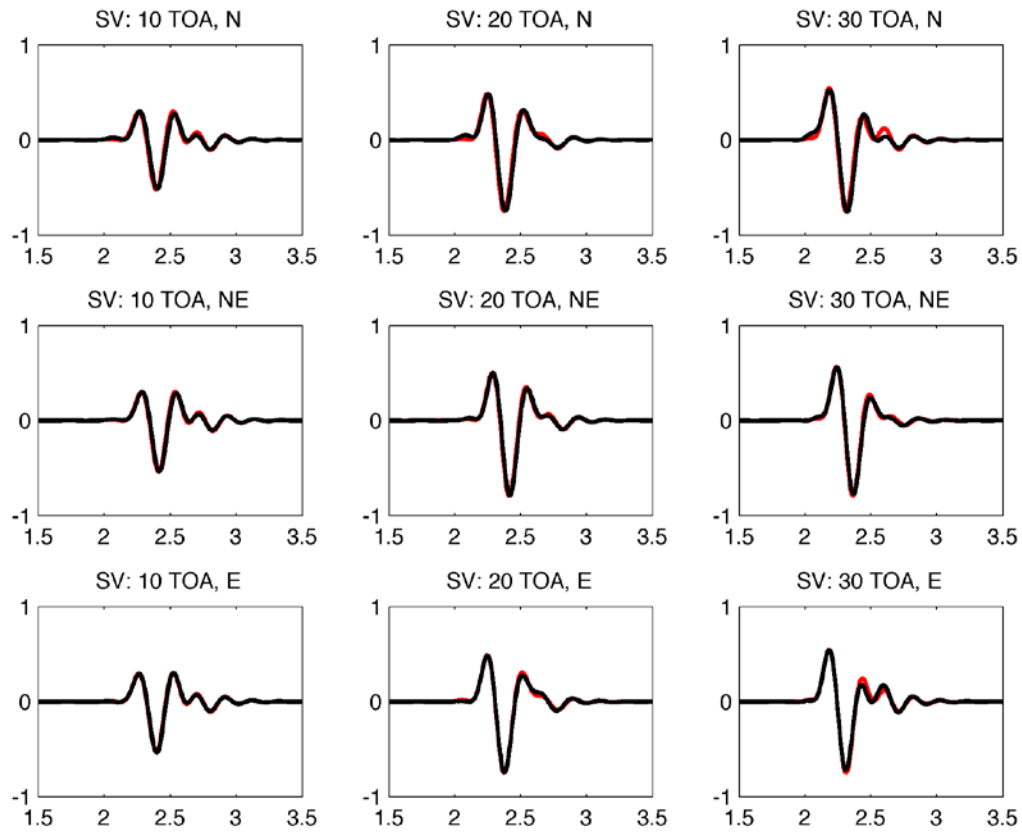


Figure 24. SV waves from Shoal calculation with tectonic release (black) and without (red). There are very small differences in the waveforms. Units are velocity normalized to  $4 \times 10^{-4}$  m/s.

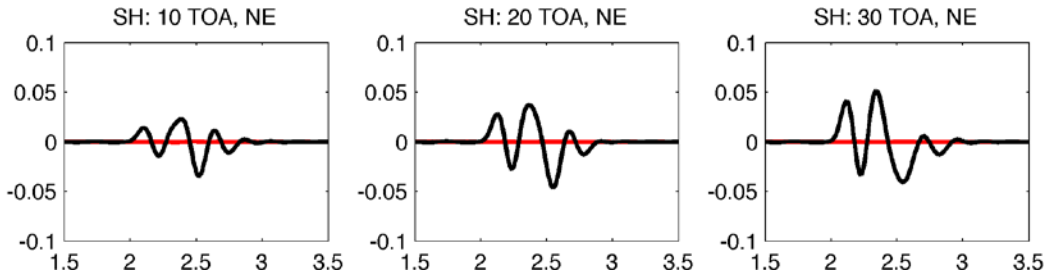


Figure 25. SH waves from Shoal calculation with tectonic release (black) and without (red). In the NE direction, a substantial SH wave is generated in the calculation with tectonic release that is not present in the calculation without tectonic release. Again, units are velocity normalized to  $4 \times 10^{-4}$  m/s, but note that the limits are different from the previous figures. The SH wave in the NE direction is about 10% the size of the SV waves. SH is zero in the north and east directions.

Although the effect of tectonic release on body wave amplitudes appears to be small, the tectonic release signal in the body wave can be identified by subtracting the body waves from the two calculations. Figure 26 shows the far field P waves along the directions of extension and compression. As expected, the extension causes an increase in signal. The tectonic signal is

about 10% the size of the direct signal and delayed slightly in time, so the peak amplitude of the signal is increased only very slightly. In the direction of compression (recall that compression was considerably weaker than extension in the other direction) the effect is smaller with the main effect being a slight amplitude decrease at about 1.9 seconds.

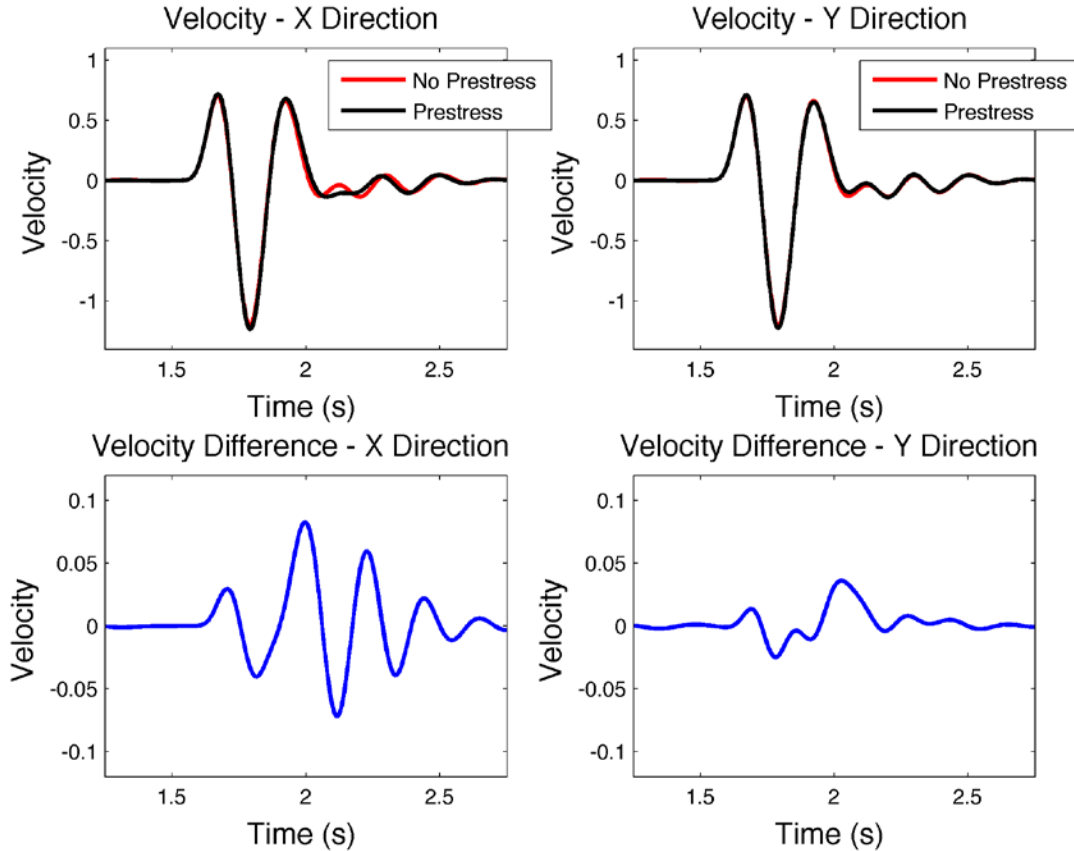


Figure 26. Top row: Far field P waves in the X and Y directions – X (North) is the direction of extension. Bottom row: Velocity differences subtracting the waveform without prestress from the waveform with prestress. Both are for a 30 degree takeoff angle. Units are velocity normalized to  $4 \times 10^4$  m/s.

The effect is similar but larger for far field SV (Figure 27), which shows that the SV waveforms from tectonic release are about 20% of the direct SV. It also starts earlier, because the “direct” SV wave is dominated by pS and so is delayed by the travel time to the surface, while the tectonic SV is coincident with the explosion. Figure 28 shows that an SH wave is generated in the calculation with tectonic release that is not present in the calculation without tectonic release. The SH wave at its maximum at 45 degrees between the Shmin and SHmax direction is about 10% the size of the SV waves. SH is zero in the direction of principal stresses which are axes of symmetry.

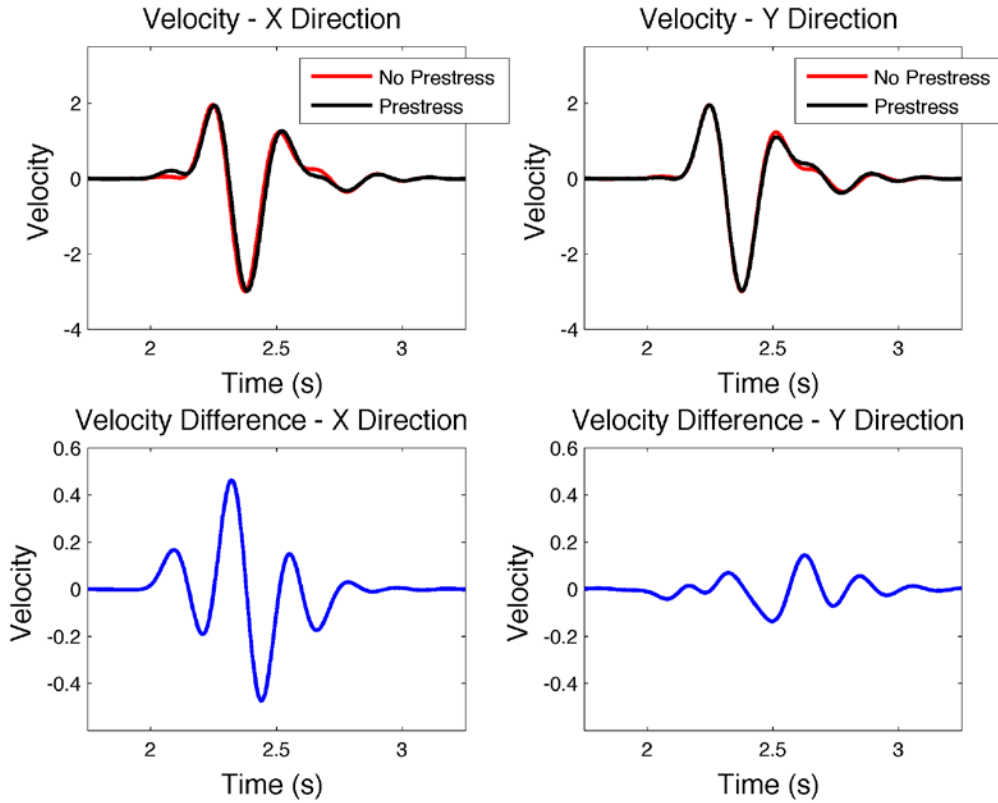


Figure 27. Top row: Far field SV waves in the X and Y directions – X (North) is the direction of extension. Bottom row: Velocity differences subtracting the waveform without prestress from the waveform with prestress. Both are for a 30 degree takeoff angle. Units are velocity normalized to  $4 \times 10^4$  m/s.

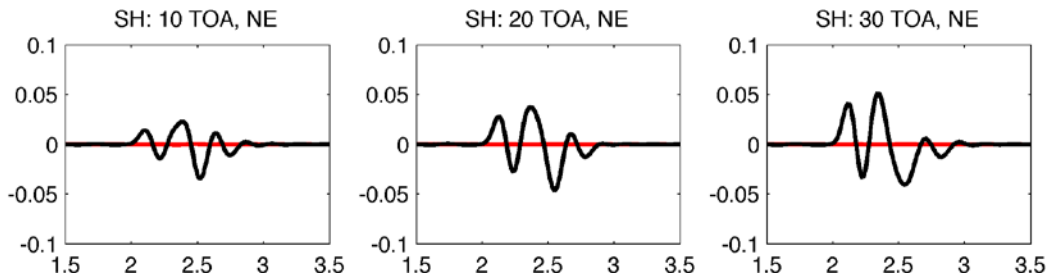


Figure 28. Far field SH-waves calculated at 10 (left), 20 (middle) and 30 (right) degree take-off angles from Shoal calculations with and without prestress; 45 degrees from the direction of extension.

In Figure 29, we compare the far field P-waves calculated for the explosion without tectonic release with a calculation for a spherically symmetric explosion source calculated in an infinite medium with the same material properties as the 3D calculation, and placed at the same depth in the same structure. The difference between these waveforms corresponds to the nonlinear effects caused by the free surface and the variation of overburden pressure with depth. These effects include spall, material damage and nonlinear deformation. The main difference is a reduction in

the pP amplitude and a longer duration in the 3D case. Similar results were found for two-dimensional calculations by Stevens et al (1991).

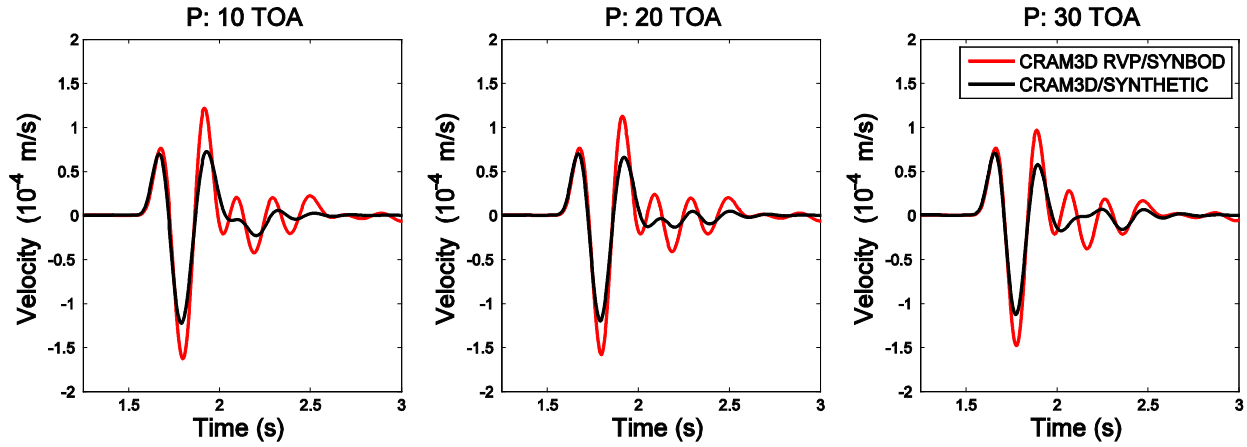


Figure 29. Far field P-waves calculated for a spherically symmetric explosion source (red) compared with far field P-waves from the Shoal calculation without tectonic release (black). Both calculations used the same material properties and earth structure. From left to right, take-off angles of 10, 20 and 30 degrees.

Figure 30 shows the same comparison for SV waves. The 3D calculation shows larger SV waves, particularly at shallower takeoff angles, and a precursor not present in the spherically symmetric case. The largest part of the SV wave is again the pS phase, modified by the nonlinear interaction with the free surface. The precursor is a direct S wave generated by the explosion in the 3D medium.

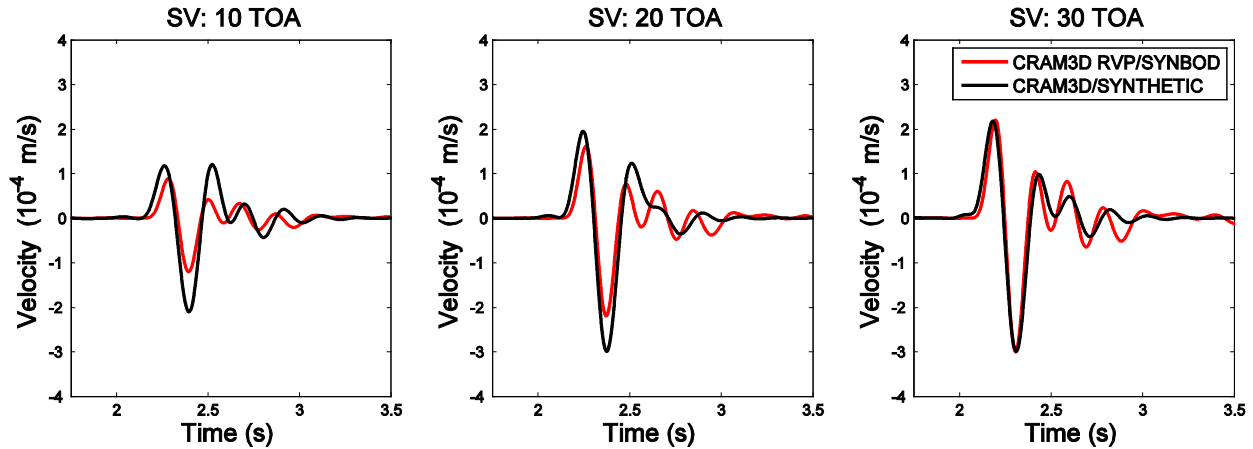


Figure 30. Far field SV-waves calculated for a spherically symmetric explosion source (red) compared with far field SV-waves from the Shoal calculation without tectonic release (black). Both calculations used the same material properties and earth structure. From left to right, take-off angles of 10, 20 and 30 degrees.

#### 4.2.5 Shoal: Hypothetical Compressive Prestress

Shoal is in a region of extension which, as shown above, increases surface wave amplitudes, although the effect is not large with the smaller compressive prestress in the other direction. In this section we consider the effects that would occur if the same explosion in the same medium were conducted in a region in compressive prestress. In this calculation, we left the secondary prestress the same and changed the dominant prestress from tensile to compressive (also rotated 90°), so the medium is balanced against friction for a thrust fault instead of a normal fault. The initial stress state for the calculation is shown in Figure 31.

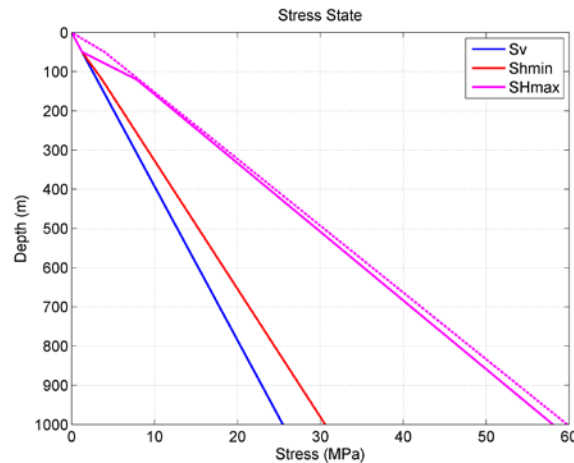


Figure 31. Stress state for calculation of Shoal with compressive prestress. The dashed line is the critical  $SH_{max}$  stress limited by friction.

The broadband regional waveforms calculated from this simulation are shown in Figure 32. At first glance they look similar to the case with tensile prestress – there is a clear Love wave and the Rayleigh wave varies with azimuth while the body waves do not, and in fact the entire wavetrain ahead of the surface waves is very similar to the other cases. Figure 33 shows the fundamental mode waveforms lowpass filtered at 0.1 Hz and compared with the same waveform for the tensile prestress case. The variation in amplitude is opposite of the tensile case. As expected, it is smallest in the direction of maximum compressive stress (90°).

Figure 34 - Figure 36 show far-field body waves from the compressive calculation compared with the other calculations. The results are very similar to the tensile prestress calculation. There is little effect on the initial waveform, but the later part of the waveform that is affected by the free surface interaction is delayed and modified by prestress. The effects described earlier are somewhat larger for compressive prestress compared to tensile prestress.

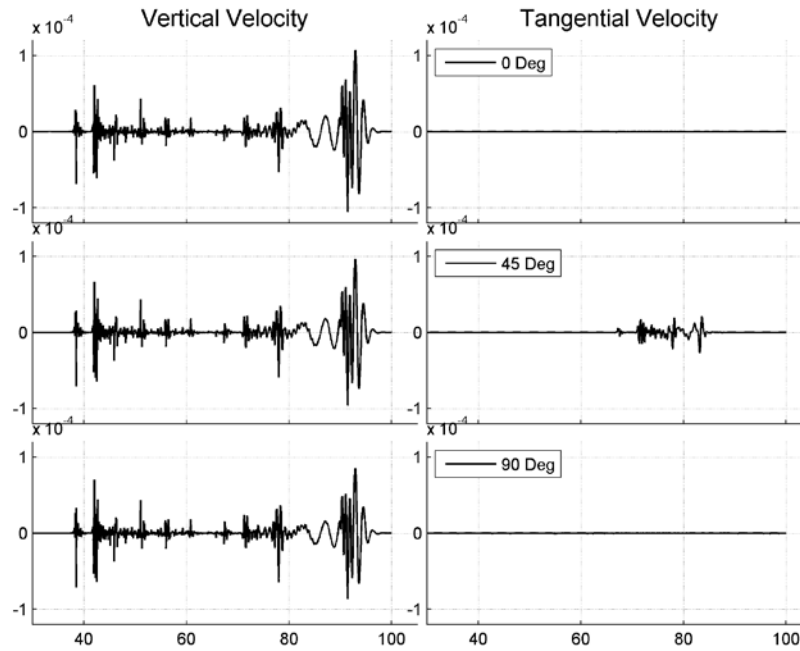


Figure 32. Broadband waveforms from the Shoal calculation with compressive prestress.

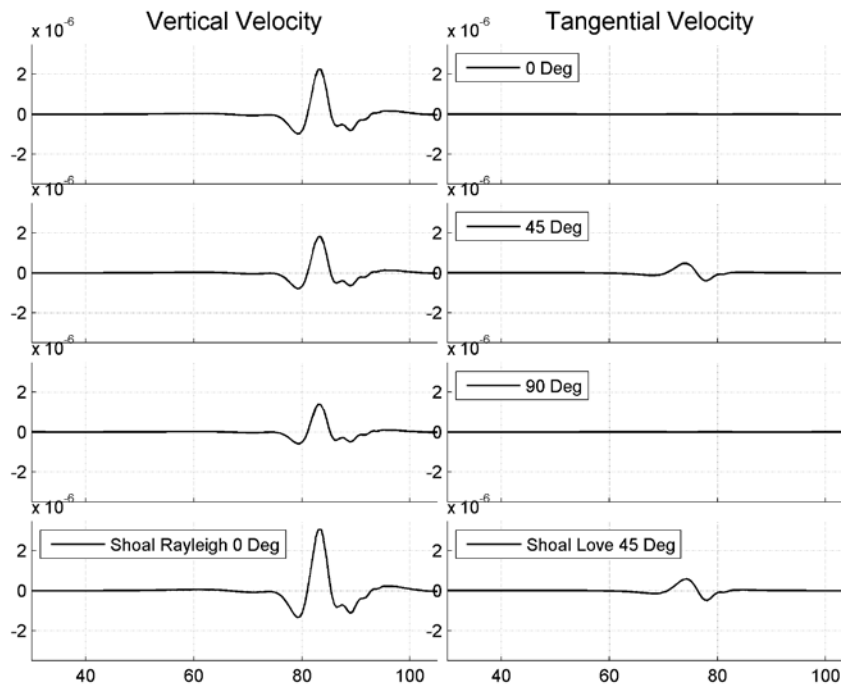


Figure 33. Fundamental mode waveforms at 250 km from the calculation with compressive prestress low pass filtered at 0.1 Hz. The bottom row shows the waveforms from the Shoal calculation described in the previous section degrees for comparison. Surface wave amplitude for the compressive case in the direction of compressive prestress is reduced.



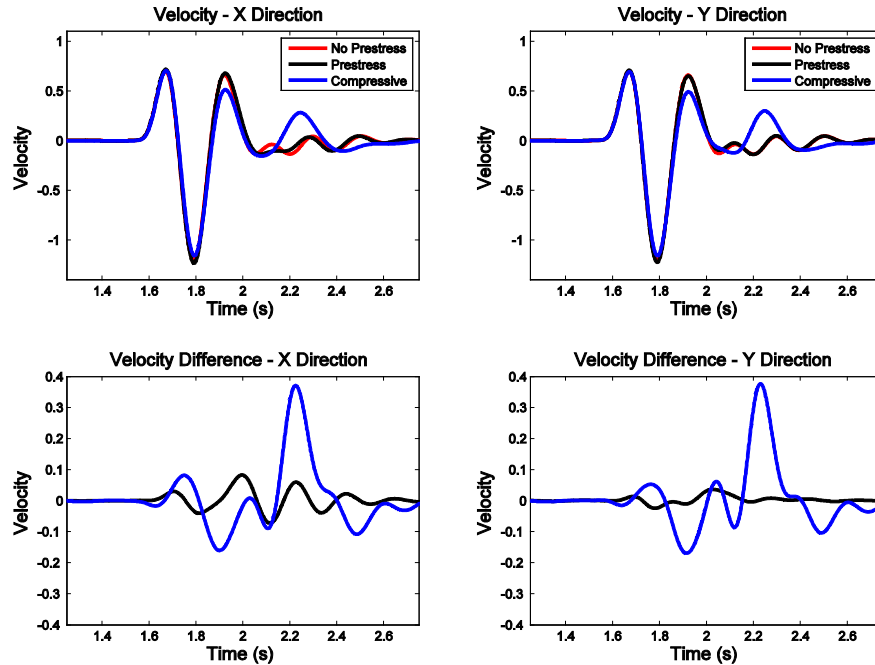


Figure 34. Top row: Far field P waves in the X and Y directions – X (North) is the direction of extension. Bottom row: Velocity differences subtracting the waveform without prestress from the waveforms with the Shoal prestress and hypothetical compressive prestress. Both are for a 30 degree takeoff angle. Units are velocity normalized to  $4 \times 10^4$  m/s.

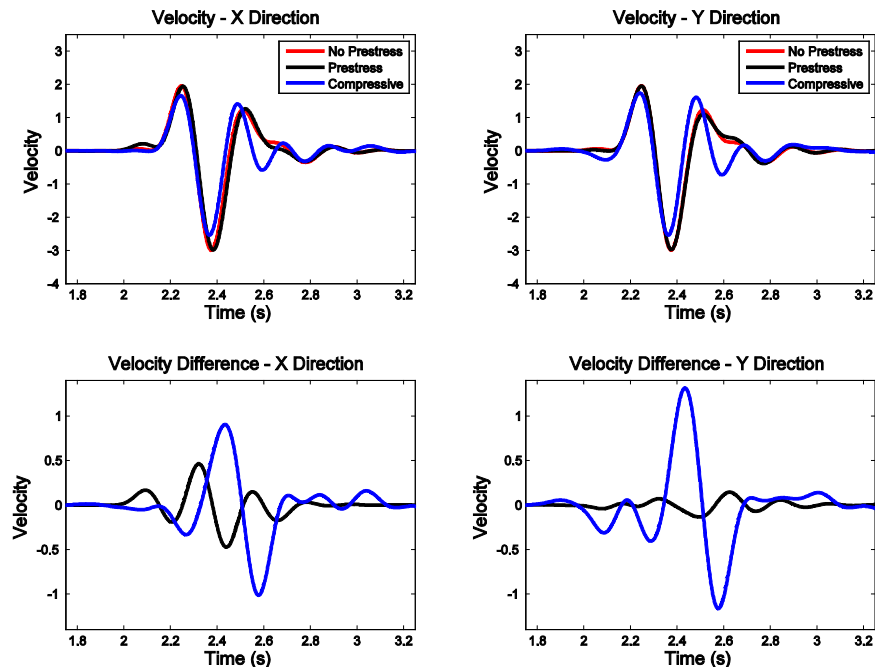


Figure 35. Top row: Far field SV waves in the X and Y directions – X (North) is the direction of extension. Bottom row: Velocity differences subtracting the waveforms without prestress from the waveforms with the Shoal prestress and hypothetical compressive prestress. Both are for a 30 degree takeoff angle. Units are velocity normalized to  $4 \times 10^4$  m/s.

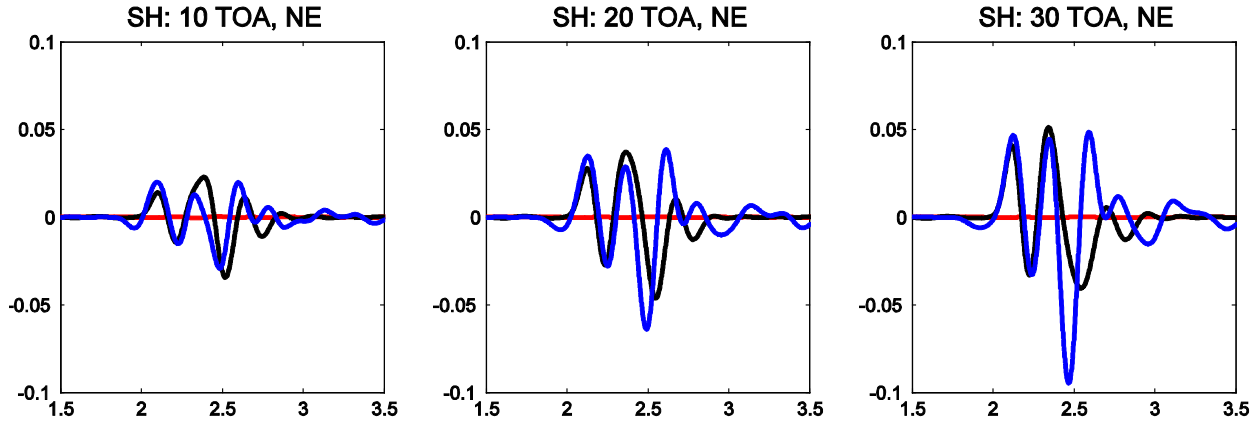


Figure 36. Far field SH-waves calculated at 10 (left), 20 (middle) and 30 (right) degree take-off angles from Shoal calculations without prestress and the waveforms with the Shoal prestress and hypothetical compressive prestress; 45 degrees from the direction of extension.

### 4.3 3D Earth Heterogeneity

All explosions generate shear waves, including even overburied and decoupled explosions. A possible explanation for this is that the extra degree of freedom provided in three dimensions makes generation of shear waves much easier than with the restriction to axisymmetric geometry. In other words, spherical and axisymmetric calculations artificially suppress the shear waves. In this section we try to estimate the magnitude of this effect by incorporating heterogeneous material properties into 3D nonlinear calculations.

The spatial distribution of the material properties of the earth's crust is composed of step-like changes and short wavelength random fluctuations, which strongly affect the propagation of elastic waves. The most difficult part is defining the characteristics of the heterogeneous media. There is very little information available on strength heterogeneity, for example. There is considerably more information available on velocity and density heterogeneity, primarily from well logs and core samples. We are using these in two ways: 1) to develop velocity and density models based on the observed distributions; and 2) to develop a strength distribution model under the assumption that the strength heterogeneity is similar to the velocity distribution.

Nine 3D finite element calculations were performed of the Shoal explosion with CRAM3D to investigate body and surface wave generation with heterogeneous material properties in the shot region (Table 3). Three pairs of the finite element calculations used distributions of density, bulk modulus, and shear modulus with statistical characteristics the same as those derived from well YT2 log data from Kyushu, Japan (Figure 37). These calculations are referred to as the "lithosphere" and "weakened lithosphere" calculations below since the material distributions are modeled after actual measurements. To test the sensitivity of the waveforms to the spatial distribution function, two calculations were performed with slightly modified spatial distributions ("modified lithosphere").

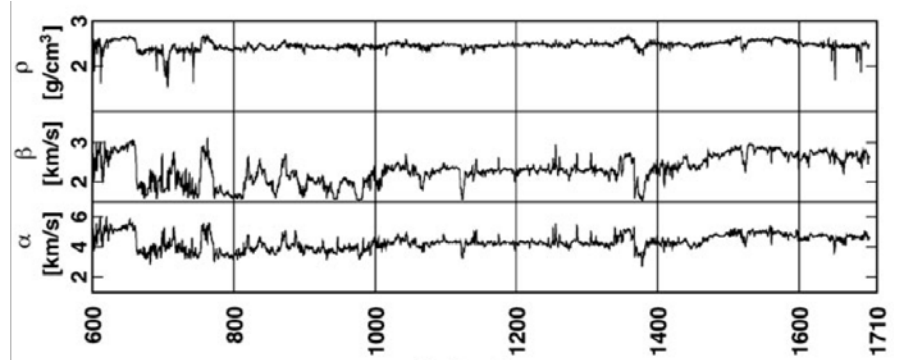


Figure 37. Taken from Shiomi et al. 1997: Well logs showing P- and S-wave velocities and mass density versus depth for well YT2 in Kyushu, Japan for depths of 600 m to 1710 m.

Table 3. Nine 3D finite element calculations were performed to investigate 3D Heterogeneity.

Calculation	Heterogeneities	Strength weakening	Number of Calcs.
Uniform media	None	No	1
Lithosphere	As in well YT2	No	3
Lithosphere (weakened)	As in well YT2	Yes	3
Modified lithosphere	Modified from YT2	No	1
Mod. lith. (weakened)	Modified from YT2	Yes	1

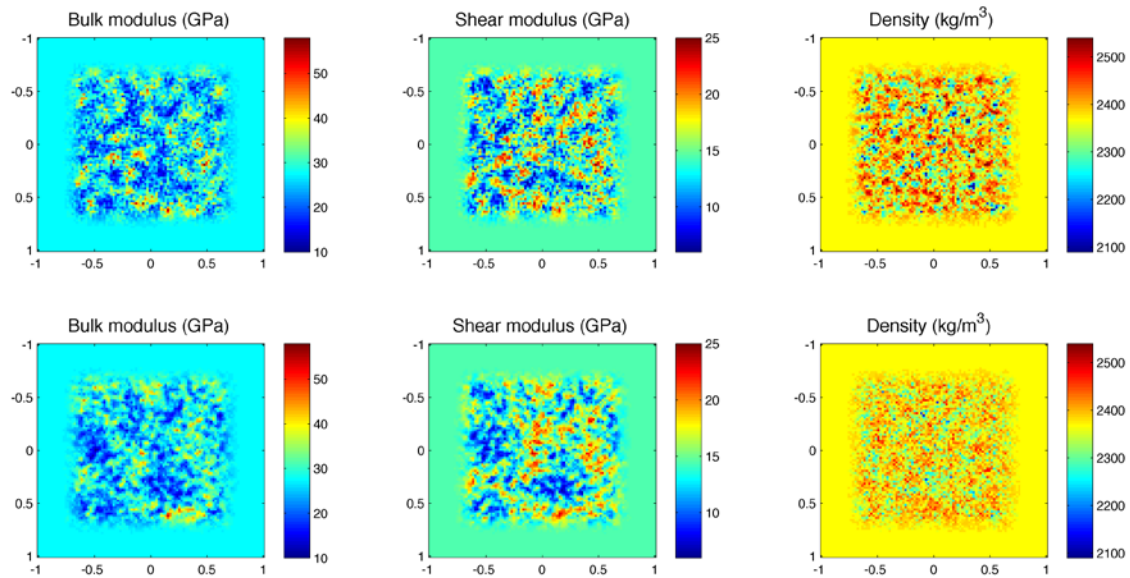


Figure 38. *Top panels*: Examples of the randomly generated material property distributions for one set of the “lithosphere” calculations for a  $2 \text{ km} \times 2 \text{ km}$  horizontal slice at 100 m depth. The resolution (cell size) of the material property distribution is 20 m. The statistical properties of these distributions are identical to those in well YT2. *Bottom panels*. Same as the top panels, but for the “modified lithosphere” calculations.

Although the YT2 well log data only reveal the distribution of material properties with depth, we assume that the same autocorrelation function applies in all spatial dimensions. Figure 38 shows horizontal slices of the material properties from two of the calculations. The top and bottom panels correspond to the spatial distribution from the YT2 well log data, and from the slightly modified distribution, respectively. The bulk modulus spans 10-58 GPa with a median value of 27.4 GPa, the shear modulus spans 6-25 GPa with a median value of 14.4 GPa, and density spans 1800-2600 kg/m<sup>3</sup> with a median value of 2370 kg/m<sup>3</sup> (Figure 39). The distributions of bulk and shear modulus are highly correlated with one another (0.92 correlation coefficient), and the density distribution is correlated to the moduli but to a lesser extent (0.31 correlation coefficient). Because of this correlation, many of local maxima in the bulk modulus distribution, for example, align with the maxima of the shear modulus distribution.

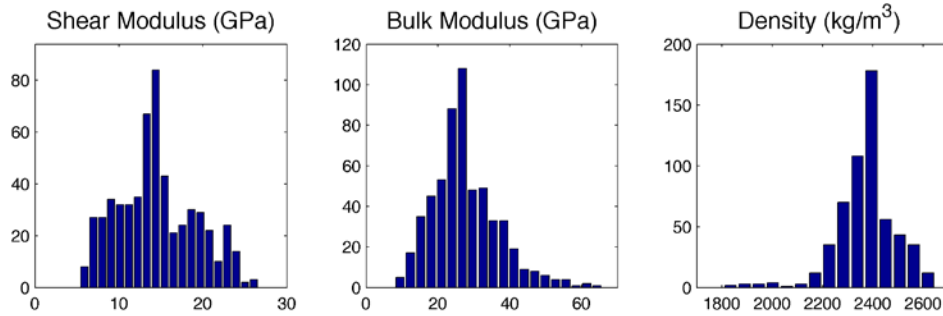


Figure 39. The distributions of the properties derived from the YT2 well log data.

The autocorrelation functions of the well log data and the two simulated distributions are shown in Figure 40. The bulk modulus and shear modulus exhibit very similar autocorrelation functions; they are spatially correlated over distances of ~80 m. The density fluctuations are correlated over distances of ~30 m. For the modified spatial distribution functions, the bulk and shear moduli are correlated over slightly larger distances, and the density is correlated over slightly smaller distances relative to the other calculations.

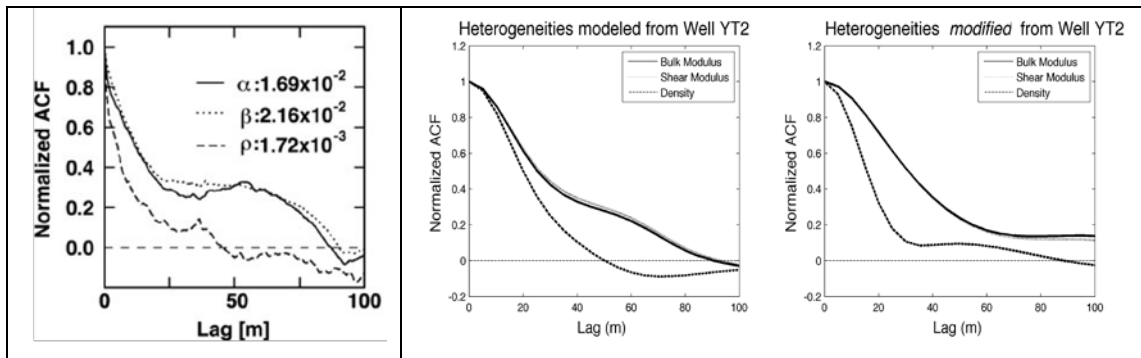


Figure 40. *Left panel:* Autocorrelation function of P wave velocity, S wave velocity, and density of the data from well YT2. The numerals are the mean-squared fractional fluctuation for each property. *Middle panel:* Ensemble average of the autocorrelation functions of bulk modulus, shear modulus, and density used in the “lithosphere” calculations. *Right panel:* Same as the middle panel, but for the “modified lithosphere” calculation.

In all the calculations, the heterogeneities are tapered to the mean values between 600 m and 800 m from the shot point along  $x$  and  $y$  dimensions, and between 200 m and 400 m below the shot point in the  $z$  dimension (heterogeneities extend to the surface). The purpose of the tapering is to have constant material properties along the monitoring surface. The monitoring surface is where the displacements and stresses are saved to propagate the wavefield from the boundary of the calculation to an arbitrary exterior observation point using the elastodynamic representation theorem.

In addition to investigating the body waves and surface waves generated from two spatial correlation functions, we also tested the effects of these distributions with the inclusion of correspondent weakening of the material properties. Material weakening (shock damage) is incorporated through a reduction in both strength and shear modulus based on the maximum shear strain seen by the rock element. Although material weakening is always included in the calculations once a minimum amount of plastic work has been surpassed, for the “weakened” calculations the reduced shear modulus and the shear strain thresholds that control the weakening are lowered. Specifically, for each cell five parameters<sup>1</sup> are all scaled by the ratio of the shear modulus in the cell to the maximum shear modulus used in the calculation (25 GPa). (See Section 1.5.3 of the CRAM3D Users Manual for a more detailed explanation of the shock damage parameters.)

Finally, we also ran a calculation with uniform material properties in order to remove the effects of the heterogeneities on the waveforms. The mean values of the varied parameters were used in this calculation.

Table 3 provides a summary of the nine 3D finite element calculations. For each calculation, body waves were calculated for take-off angles of 10, 20, and 30 degrees along 4 azimuths (to the north, east, south, and west). Surface waves were calculated for 4 azimuths.

### **4.3.1 Heterogeneous Source Region: Far Field Body Waves**

The body waveforms for the “lithosphere” and the “weakened lithosphere” calculations are shown in Figure 41. In addition, we show the “lithosphere” body waves with the “uniform” body waves subtracted to try to isolate the effects of the heterogeneities. Root-mean-squared (RMS) amplitudes of the body waves were calculated using 2 seconds of data containing the entire waveforms (Table 4).

<sup>1</sup> deinit, defull, epinit, eptfull, gdam; See the CRAM3D Users Manual.

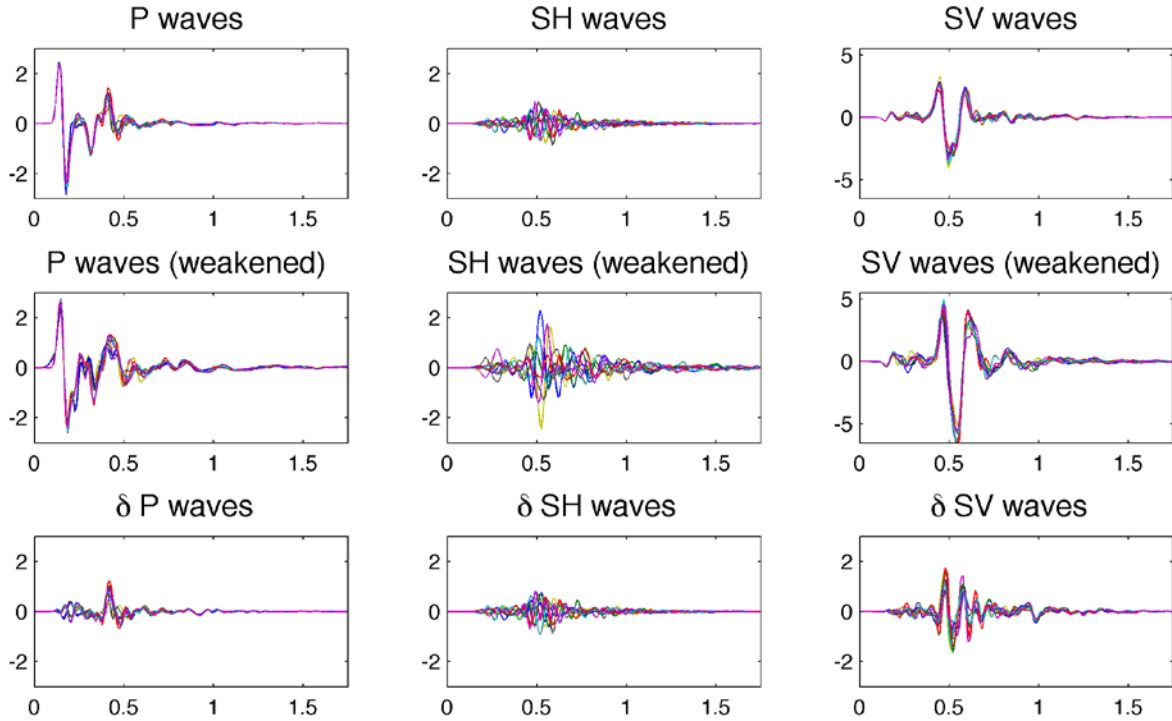


Figure 41. *Top*: Body waves for a 10 degree take-off angle, low-pass filtered at 20 Hz, for 4 directions for each of the 3 “lithosphere” calculations. The amplitudes of the waveforms are scaled by  $1e-4$  and are for 1000 km range. Time is on the  $x$ -axis; a negative offset of 0.333 s has been applied to the shear waves to align the start of the motion. *Middle*: Same as the top panel, but for the 3 “weakened lithosphere” calculations. *Bottom*: Same as the top panels, but with the “uniform” media calculation subtracted from the waveforms.

Including heterogeneity in the material properties of the source region has only a subtle effect on the RMS amplitudes of P and SV waves (1-6 percent increases relative to uniform media). SH waves, which are non-existent in uniform media, are generated with RMS amplitudes about 20-33 percent as large as SV waves. When concurrent weakening of the material is also included, the RMS amplitudes for all body wave types are increased on average. P wave amplitudes increase 10-20 percent relative to uniform and heterogeneous cases without weakening. SH amplitudes increase substantially, by 70-150 percent. The RMS amplitudes of SV waves also increase nearly 70-80 percent for a 10 degree take off angle, but the amplification from material weakening is greatly diminished at larger take off angles, with only about 10 percent increase at a 30 degree take-off angle.

Table 4. RMS amplitudes of body waves for the nine CRAM3D calculations.

Calculation	P10	P20	P30	SH10	SH20	SH30	SV10	SV20	SV30
Uniform	4.19	4.09	3.98	0	0	0	6.53	8.46	7.58
Lithosphere 1	4.41	4.19	3.98	1.37	1.16	1.21	6.70	8.41	7.54
Lithosphere 2	4.43	4.16	3.97	1.36	1.17	1.22	6.76	8.42	7.55
Lithosphere 3	4.26	4.07	3.88	1.28	1.44	1.23	6.88	8.24	7.21
Modified lith. 1	4.32	4.17	4.00	1.77	1.62	1.59	5.96	7.93	7.32
Lith. 1 (weakened)	5.13	4.74	4.42	2.34	2.82	2.11	12.23	9.67	8.45
Lith. 2 (weakened)	5.09	4.70	4.42	2.33	2.81	2.09	12.19	9.68	8.46
Lith. 3 (weakened)	4.76	4.82	4.62	3.19	2.48	2.24	11.87	9.90	8.49
Mod. lith. 1 (wknd)	4.95	4.70	4.48	3.10	3.62	2.70	10.70	9.27	8.15

Note.—RMS amplitudes for P, SH, and SV waves at 10, 20, and 30 degree take-off angles. Each measurement is derived from the average of 4 azimuths (north, east, south, west). Amplitudes are scaled by  $1e-5$ .

Because P and SV waves are present even in the absence of heterogeneity, only subtle differences with azimuth are observed. The largest differences in the waveforms occur where the gradient of the waveform is largest (Figure 41, bottom), indicating that the waves are primarily affected by propagation speed fluctuations. Similarly, the particular random instance drawn from the “lithosphere” or “modified lithosphere” distribution functions (1, 2, or 3) has a relatively minor effect on the P and SV waves. On the contrary, SH waves show ~20-30% variation in RMS amplitude with azimuth.

Table 5. Azimuthal variation (percent) of body waves in the presence of heterogeneity ( $1\sigma$ )

Calculation	P10	P20	P30	SH10	SH20	SH30	SV10	SV20	SV30
Lithosphere	2	2	3	13	19	21	6	4	4
Modified lith.	1	3	5	18	16	27	7	8	4
Lith. (weakened)	3	2	3	25	17	18	7	9	3
Mod. lith. (wknd)	1	3	3	33	11	5	3	3	2

Note.—Tabulation of the percent variation with azimuth combines the 3 “lithosphere” and “weakened lithosphere” calculations (12 azimuths).

The power spectral density of the waveforms for P and SV waves are only slightly different in the “weakened” calculations relative to the non-weakening calculations (Figure 42). Both types of waveforms show a subtle shift of energy from high frequencies to lower frequencies. SH waves, on the other hand, show a more distinct shift in energy to longer periods.

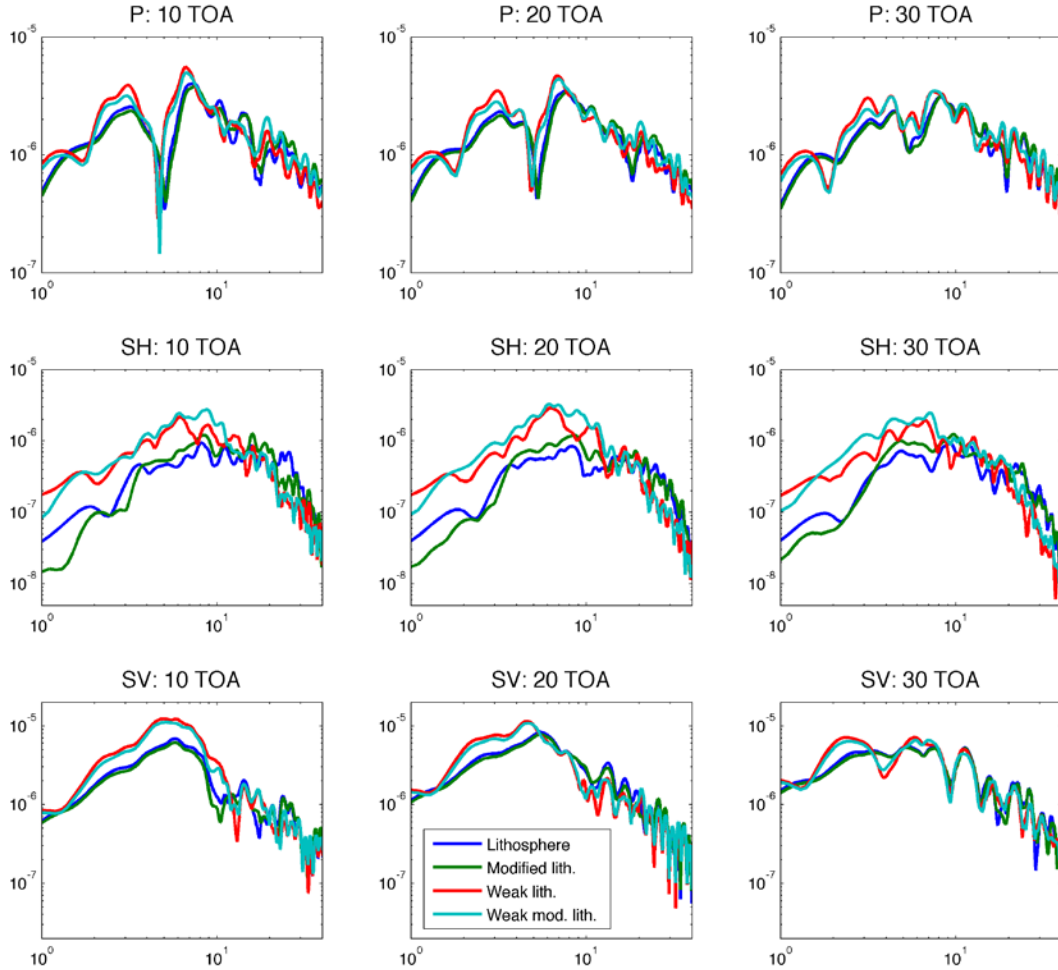


Figure 42. Normalized power spectral density of the body waves for the 4 types of scenarios under investigation. Distinct wave types (take-off angles) are shown in each row (column).

#### 4.3.2 Heterogeneous Source Region: Broadband Waveforms and Surface Waves

Broadband regional waveforms at 250 km were calculated from the nine CRAM3D calculations. As seen in Table 6, heterogeneous material properties in the source region (without weakening) generate Love waves, but have only a small effect on the Rayleigh waves. However, the RMS amplitudes of the Love waves are  $\sim 3\times$  greater when enhanced weakening of the material properties is included in the calculations. Rayleigh wave amplitudes increase a more modest  $\sim 40\%$  with weakening. Comparison of Figure 43 and Figure 44 clearly reveals the significant increase in surface wave amplitudes with material weakening. Similar to SH waves, the standard deviation of the RMS amplitudes of the Love waves over all azimuths is about 20%, independent of whether or not enhanced material weakening is included in the calculation. The variation with azimuth of the Rayleigh waves is very small ( $\sim 3\%$ ) in all heterogeneity cases.



Table 6. Surface waves with uniform and heterogeneous material properties in the source region.

Calculation	Love waves RMS amplitudes	Love waves percent variation with azimuth ( $1\sigma$ )	Rayleigh waves (vertical)	Rayleigh waves percent variation with azimuth ( $1\sigma$ )
Uniform	0	0	136	0
Lithosphere	5.5	16	137	2
Modified lith.	5.5	18	127	2
Lith. (weakened)	16.4	17	209	3
Mod. lith. (wknd)	17.9	19	192	3

Note.—RMS amplitudes are calculated from 20 s of data enclosing the waveforms (67-87 s for Love waves, 80-100 s for Rayleigh waves). Waveforms are low-pass filtered at 2 Hz. RMS amplitudes are for a 250 km range and are scaled by  $1e-7$ . The percent variation in wave amplitude is calculated from 12 directions (4 directions in each of 3 independent calculations) for the “lithosphere” calculations and 4 directions from the “modified lithosphere” calculations.

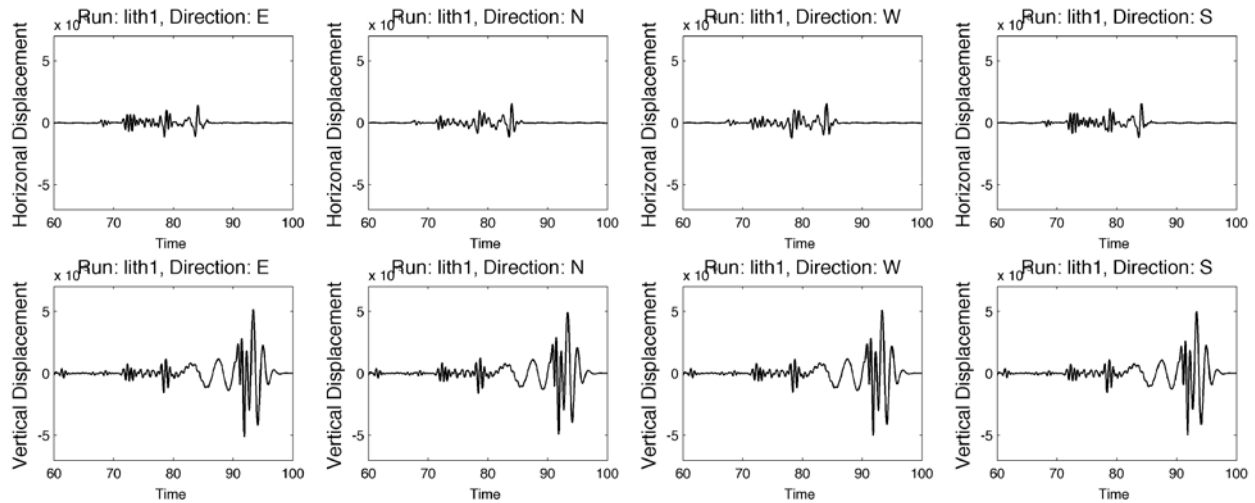


Figure 43. Surface wave displacements in 4 directions at 250 km range for the “lithosphere 1” calculation. The waveforms are low-pass filtered at 2 Hz. The y-axis is measured in units of  $1e-6$  m for horizontal displacements and  $1e-7$  m for vertical displacements.

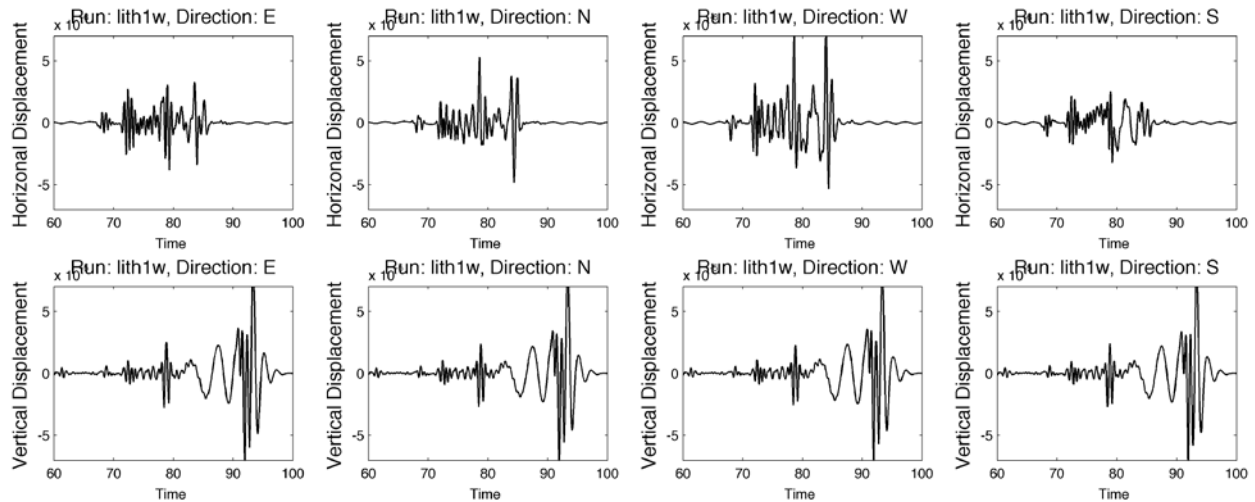


Figure 44. Same as Figure 43, but for the “lithosphere 1 (weakened)” calculation.

The power spectral density of the surface waveforms is shown in Figure 45. Similar to the body waves, there are nearly negligible differences between the spectra of the “lithosphere” and “modified lithosphere” calculations. On the other hand, the inclusion of enhanced material weakening in the calculations generates a more noticeable change. In the case of body waves the spectra have maximal power near ~4-8 Hz, while in the case of surface waves the spectra peak near ~0.4-1.0 Hz.

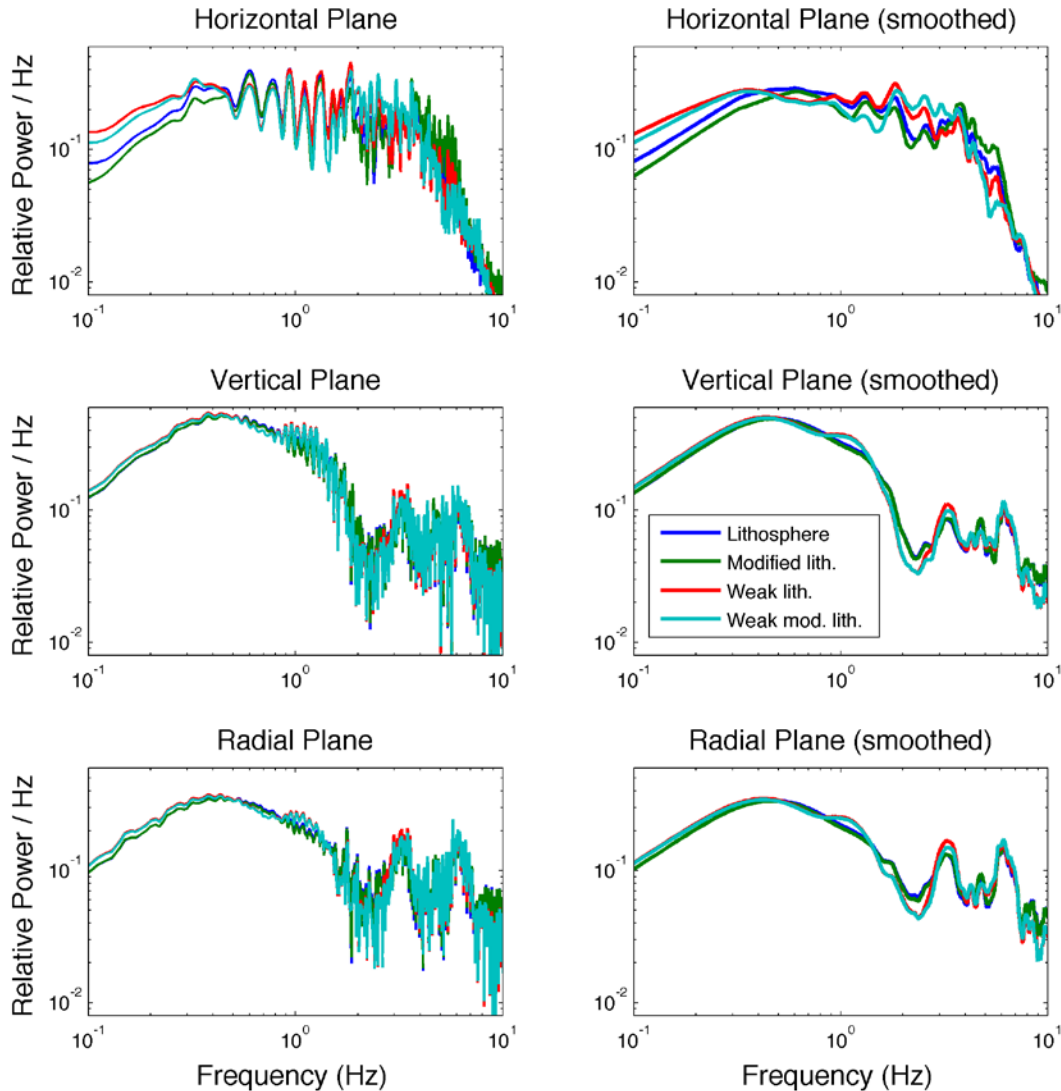


Figure 45. Normalized power spectral density of the surface waves for displacements in the horizontal, vertical, and radial planes (top to bottom). The right panel shows the power spectra after smoothing in frequency, created by averaging the power in adjacent frequency bins to more clearly show the spectral differences between the waveforms.

The difference between the spectra with and without enhanced weakening is presented in Figure 46. As with body waves, the high frequency spectra are relatively unchanged. For displacements along all three directions, material weakening increases the power at frequencies below ~0.5 Hz

and between ~0.8-1.5 Hz, and decreases the power at frequencies between ~0.5-0.8 Hz. Above 1.5 Hz, the change in the spectra for horizontal displacements relative to vertical and radial displacements are opposite in sign. Horizontal displacements are enhanced from 1.5 Hz to 3 Hz, and are reduced from ~3-7 Hz. Vertical/radial displacements are reduced from 1.5 Hz to 3 Hz, and are enhanced from ~3-7 Hz.

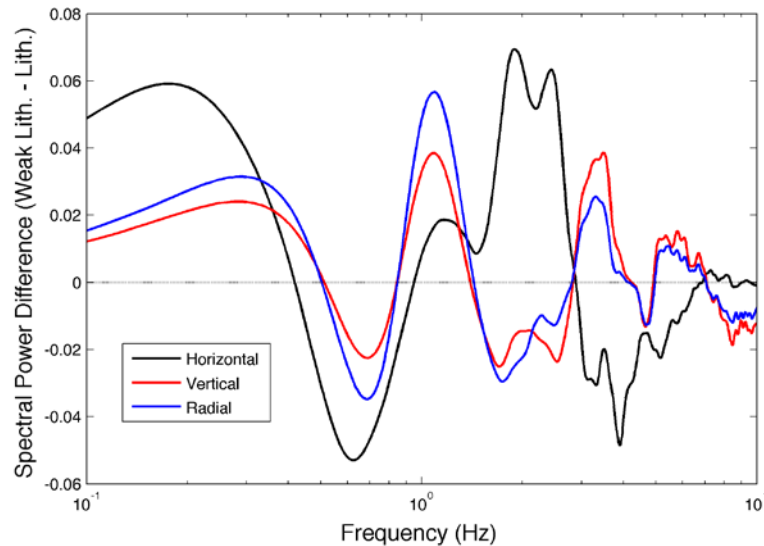


Figure 46. Difference in normalized spectral power for the surface waves with and without enhanced material weakening.

### 4.3.3 Heterogeneous Source Region: Nonlinear Deformation

In uniform media, symmetry ensures that nonlinear deformation generated by the explosion is axisymmetric along any horizontal plane (Figure 47). In this case, yielding is confined to a spherical region ~150-200 m surrounding the shot point, in addition to a broader area near the surface resulting from spall. With heterogeneous material properties, the axisymmetry is broken which enhances the nonlinear deformation (Figure 48 and Figure 49). Rather than being confined to the surface and a spherical volume surround the explosion, the non-linear deformation generated by an explosion in heterogeneous media extends through ~10-100 m filaments from the shot region to the surface. In some cases, heterogeneity generates channels of deformed material emanating up to 400 m from the source region (e.g., Figure 48, *middle-right*). Weakening of the material properties has a marginal (enhancing) effect on the extent of nonlinear deformation.

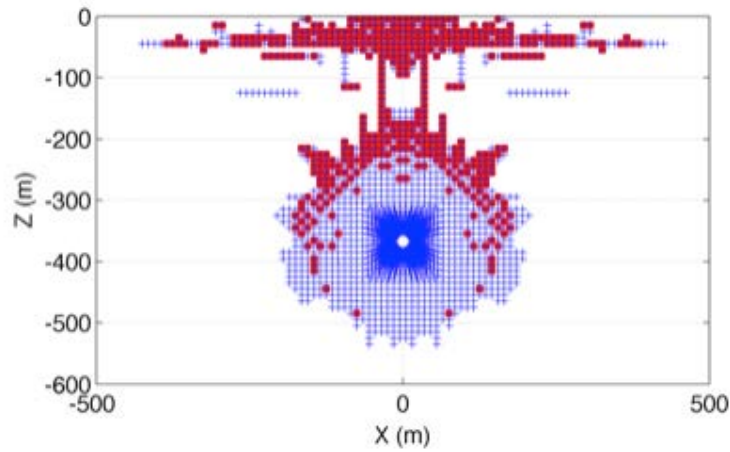


Figure 47. Vertical plane through the shot point showing nonlinear damage in the source region comprised of uniform material properties. Cells that have yielded are shown in blue, and cells that have cracked are shown in red.

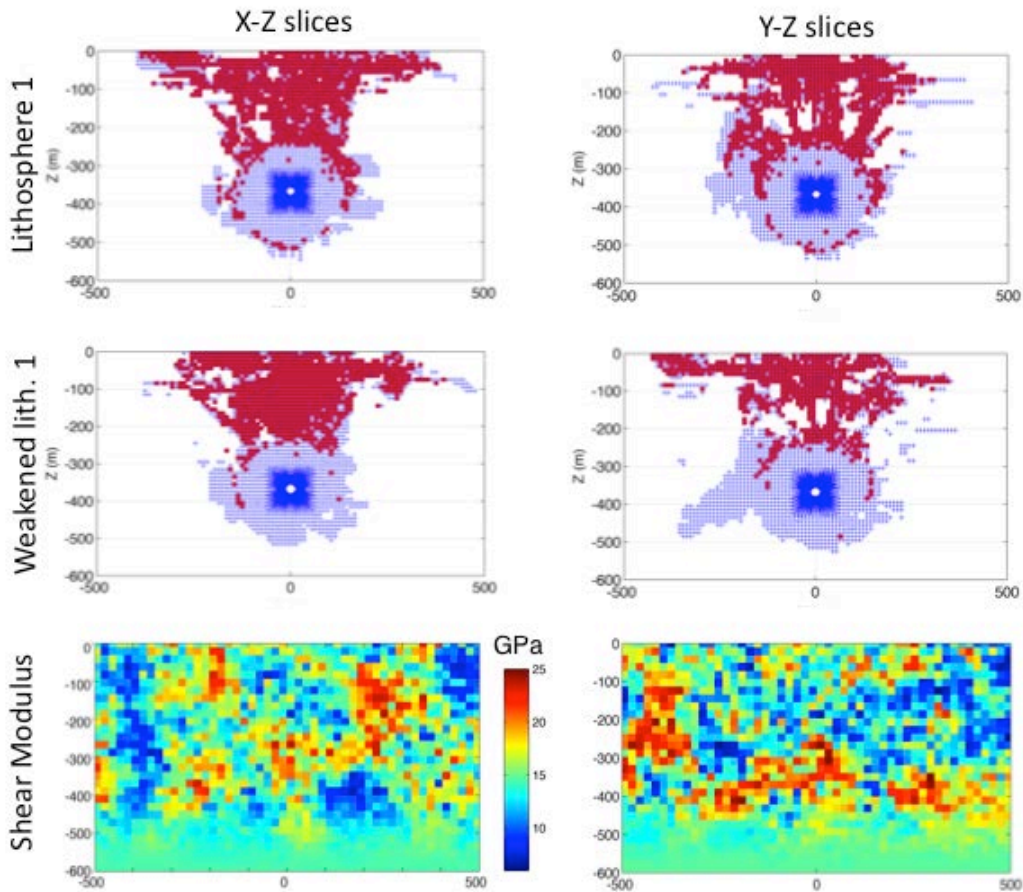


Figure 48. *Top* and *middle* panels: Vertical plane through the shot point showing nonlinear deformation in the source region for the “lithosphere 1” and “lithosphere 1 (weakened)” calculations, respectively. *Bottom* panel: Vertical plane through the shot point showing the shear modulus.

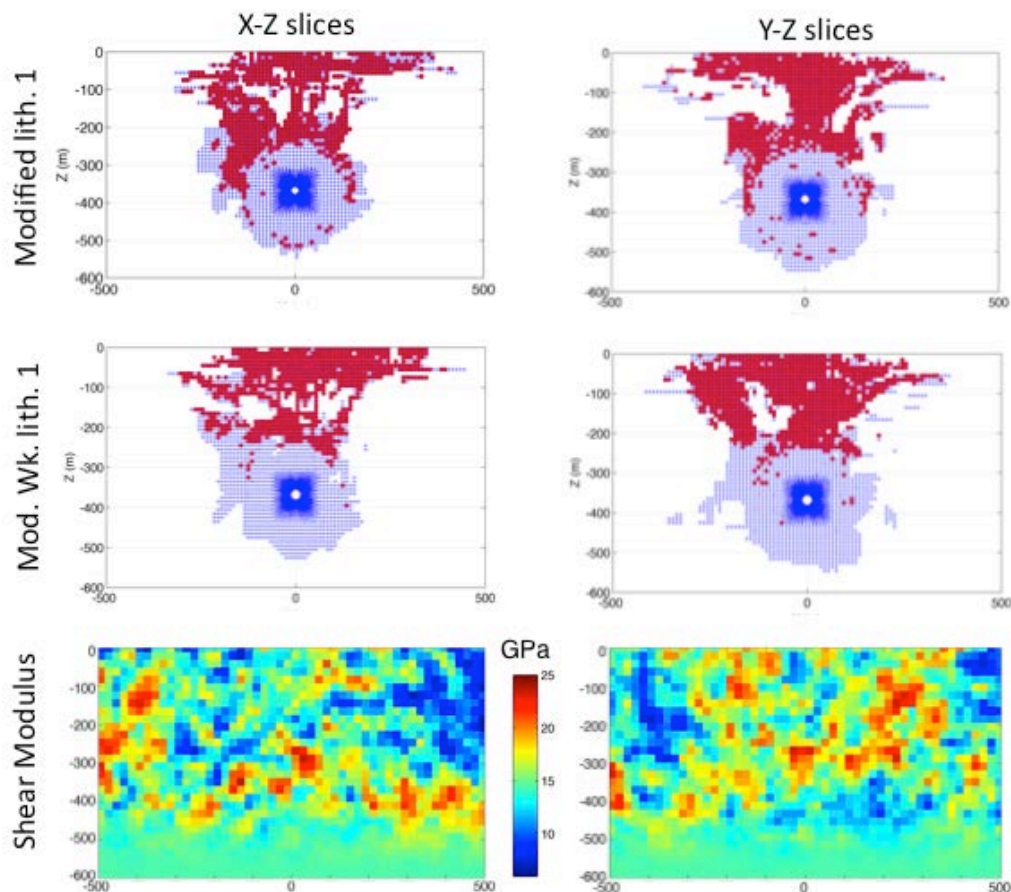


Figure 49. Same as Figure 48, but for the "modified lithosphere 1" calculations.

When enhanced weakening is included in the calculations, the weakest material regions exhibit greater nonlinear deformation. Figure 50 shows regions of enhanced weakening relative to regions of nonlinear deformation for two of the calculations. In each case, the area of nonlinear deformation has an irregular outline, but some of the larger protrusions extend into the weaker regions where they abut a stronger patch of material.



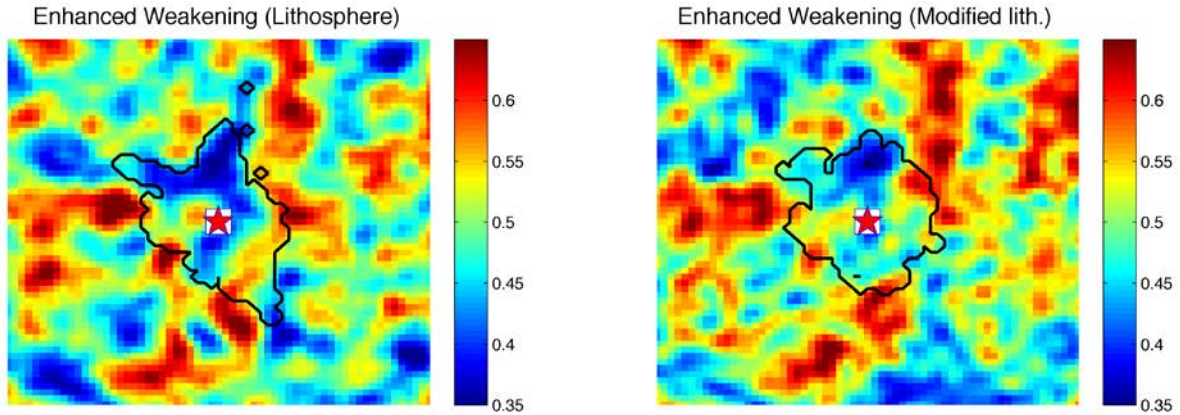


Figure 50. Regions of enhanced weakening (smoothed with a Gaussian kernel of 20 m half-width) for the “lithosphere 1” calculation (left) and the “modified lithosphere 1” calculation (right) in the  $x$ - $y$  plane at shot depth. Overlaid on top of the images are contours enclosing the regions of nonlinear deformation. Each image is 600 m on a side. Colors span 0.35 to 0.65, indicating the fractional strength of the material relative to the non-weakened calculations.

## 5. CONCLUSIONS

In this project we are trying to understand the effects of 3D structural variations on seismic waves from underground explosions. One of the main objectives is to understand why shear waves generated by underground explosions are ubiquitous. We have performed calculations with variable strength distribution, topography and 3D tectonic strain release, and modeled the SHOAL and NPE explosions. We have run a calculation of the NPE with and without topography, and extended the calculation to 400 km using the representation theorem. The calculation shows that the effect of topography can be modeled and produces effects consistent with the data. Near field tangential motion is caused primarily by topographic gradients. The effects of near-source topography on subsurface ground motion is primarily due to off-axis propagation. The effects of near-source topography on far-field seismic radiation are small.

The calculation of SHOAL shows that tectonic strain release consistent with the local stress state can generate near field and regional signals, including long period surface waves, similar to those observed. We find that tectonic release causes small changes to the far-field P-wave waveform, but has very little effect on far-field P-wave amplitudes. It does generate SH waves not present in the calculation without tectonic release. This implies that while tectonic release may significantly affect  $M_s$ , the effect on  $m_b$  will be small. The calculated effects of tectonic release are similar to those observed, but not quite as large. This probably means that the in-situ material which is nearly critically balanced against tectonic stresses is initially weaker than the material model used in the calculation which is stronger until failure occurs. An initially weaker material would amplify the effects that we observed in our calculations. It is very likely that the observed near field motion and Love waves and Rayleigh wave variations were due to tectonic strain release.

The calculations with 3D heterogeneity show that both elastic heterogeneity and strength heterogeneity cause generation of shear waves, in particular SH motions, however the effect is much stronger when strength variation is included. Strength variability leads to odd-shaped regions of nonlinear deformation that enhance shear wave generation.

## REFERENCES

- Apsel, R. J. and J. E. Luco (1983), On the Green's Functions for a layered half-space, Part II, *Bull. Seismol. Soc. Am.* **73**, pp. 931-951.
- Archambeau, C. B. (1972), The theory of stress wave radiation from explosions in prestressed media, *Geophys. J.* **29**, pp. 329-366.
- Bache, T. C. and D. G. Harkrider (1976), The body waves due to a general seismic source in a layered earth model, *Bull. Seismol. Soc. Am.* **66**, pp. 1805-1819.
- Bache, T. C., S. M. Day, and H. J. Swanger (1982), Rayleigh wave synthetic seismograms from multi-dimensional simulations of underground explosions, *Bull. Seismol. Soc. Am.* **72**, pp. 15-28.
- Beers, R. F. (1964), Analysis of Shoal Data on Ground Motion and Containment, VELA Uniform Report VUF-1013, December.
- Day, S. M., J. T. Cherry, N. Rimer, and J. L. Stevens (1987), Nonlinear model of tectonic release from underground explosions, *Bull. Seismol. Soc. Am.* **77**, pp. 996-1016.
- Kamm, J. R. and R. J. Bos (1995), Comparison of chemical and nuclear explosions: numerical simulations of the non-proliferation experiment, Los Alamos National Laboratory report LA-12942-MS.
- Lambert, Flynn and Archambeau (1972), A comparative study of the elastic wave radiation from earthquakes and underground explosions, *Geophys. J. R. Astr. Soc.* **29**, pp. 403-432.
- Liu, L. and M. D. Zoback (1992), The effect of topography on the state of stress in the crust: application to the site of the Cajon Pass Scientific Drilling Project, *J. Geophys. Res.* **97**(B4), pp. 5095-5108, doi:10.1029/91JB01355.
- Luco, J. E. and R. J. Apsel (1983), On the Green's Functions for a layered half-space, Part I, *Bull. Seismol. Soc. Am.* **73**, pp. 909-929.
- Murphy, J. R., J. L. Stevens, B. C. Kohl, T. J. Bennett, and B. W. Barker (2011), Supplemental analyses of the seismic characteristics of the 2006 and 2009 North Korean nuclear tests, in *Proceedings of the 2011 Monitoring Research Review: Ground-Based Nuclear Explosion Monitoring Technologies*, LA-UR-11-04823, Vol. 1, pp. 513-523.
- Murphy, J. R., J. L. Stevens, B. C. Kohl, and T. J. Bennett (2013), Advanced seismic analyses of the source characteristics of the 2006 and 2009 North Korean nuclear tests, *Bull. Seism. Soc. Am.* **103**, No. 3, pp. 1640-1661, doi: 10.1785/0120120194.
- Myers, Stephen C., Jeffery L. Wagoner, and Shawn C. Larsen (2007), Numerical experiments investigating the source of explosion S-waves, in *Proceedings of the 29th Annual Monitoring Research Review: Ground-Based Nuclear Explosion Monitoring Technologies*, LA-UR-07-5613, Vol. 1, pp. 175-184.

- Patton, H. J. and S. R. Taylor (2011), The apparent explosion moment: Inferences of volumetric moment due to source medium damage by underground explosions, *J. Geophys. Res.* **116**, B03310, doi:10.1029/2010JB007937.
- Rimer, N., W. Proffer, E. Halda, and R. Nilson (1994), Containment related phenomenology from Chemical Kiloton, Maxwell Laboratories technical report to Defense Nuclear Agency, SSS-DTR-94-14405.
- Rygg, E. (1979), Anomalous surface waves from underground explosions, *Bull. Seismol. Soc. Am.* **69**, pp. 1995-2002.
- Shiomi, K., H. Sato, and M. Ohtake (1997), Broadband power-law spectra of well-log data in Japan, *Geophys. J. Int.* **130**, pp. 57-64.
- Stevens, J. L., T. G. Barker, S. M. Day, K. L. McLaughlin, N. Rimer, and B. Shkoller (1991), Simulation of teleseismic body waves, regional seismograms, and Rayleigh wave phase shifts using two-dimensional nonlinear models of explosion sources, AGU Geophysical Monograph 65: Explosion Source Phenomenology, S. Taylor, H. Patton, P. Richards, editors, ISBN 0-87590-031-3, pp. 239-252.
- Stevens, J. L., N. Rimer, H. Xu, G. E. Baker, and S. M. Day (2003), *Near field and regional modeling of explosions at the Degelen Test Site*, SAIC-02/2050, Science Application International Corporation, San Diego, CA, January.
- Stevens, J. L., G. E. Baker, H. Xu, T. J. Bennett, N. Rimer, and S. M. Day (2004), *The physical basis of Lg generation by explosion sources*, OSTI ID: 835251, Science Application International Corporation, San Diego, CA, December.
- Stevens, Jeffery L. and Heming Xu (2010), Wave propagation from complex 3D sources using the representation theorem, in *Proceedings of the 2010 Monitoring Research Review: Ground-Based Nuclear Explosion Monitoring Technologies*, LA-UR-10-05578, Vol. 1, pp. 519-528.
- Stevens, Jeffery L., Heming Xu, Michael O'Brien, Walter Nagy, and Norton Rimer (2011), *Wave propagation from complex 3D sources using the representation theorem*, AFRL-RV-HA-TR-2011-1019, Science Application International Corporation, San Diego, CA, March.
- Stevens, J. L., M. O'Brien, H. Xu, and N. Rimer (2014), *User Manual for the CRAM3D Finite Element Code, Version 2.0*, 14/3002, Leidos, San Diego, CA, April.
- Toksoz, N. and H. Kehrner (1972), Tectonic strain release by explosions and its effect on discrimination, *Geophys. J. R. Astr. Soc.* **31**, pp. 141-161.
- Weart, Wendell D. (1965), *VELA UNIFORM, Project SHOAL, Project 1.1, Free Field Earth Motion and Spalling Measurements in Granite*, VUF-2001, Sandia Corporation, Albuquerque, NM, February.
- Zoback, M. D. (2010), *Reservoir Mechanics*, Cambridge University Press.



## **LIST OF SYMBOLS, ABBREVIATIONS, AND ACRONYMS**

AFRL	Air Force Research Laboratory
AFSPC	Air Force Space Command
AFWA	Air Force Weather Agency
NPE	Non-proliferation Experiment

## **DISTRIBUTION LIST**

DTIC/OCF	
8725 John J. Kingman Rd, Suite 0944	
Ft Belvoir, VA 22060-6218	1 cy
AFRL/RVIL	
Kirtland AFB, NM 87117-5776	2 cys
Official Record Copy	
AFRL/RVBYE/Robert Raistrick	1 cy